ΕΘΝΙΚΟ ΜΕΤΣΟΒΙΟ ΠΟΛΥΤΕΧΝΕΙΟ
ΣΧΟΛΗ ΗΛΕΚΤΡΟΛΟΓΩΝ ΜΗΧΑΝΙΚΩΝ
ΚΑΙ ΜΗΧΑΝΙΚΩΝ ΥΠΟΛΟΓΙΣΤΩΝ
ΤΟΜΕΑΣ ΣΥΣΤΗΜΑΤΩΝ ΜΕΤΑΔΟΣΗΣ ΠΛΗΡΟΦΟΡΙΑΣ ΚΑΙ
ΤΕΧΝΟΛΟΓΙΑΣ ΥΛΙΚΩΝ

DEUTCHES ZENTRUM FÜR LUFT- UND RAUMFAHRT
ΓΕΡΜΑΝΙΚΟ ΑΕΡΟΔΙΑΣΤΗΜΙΚΟ ΚΕΝΤΡΟ
ΙΝΣΤΙΤΟΥΤΟ ΕΠΙΚΟΙΝΩΝΙΩΝ ΚΑΙ ΠΛΟΗΓΗΣΗΣ
ΤΜΗΜΑ ΨΗΦΙΑΚΩΝ ΔΙΚΤΥΩΝ
ΟΜΑΔΑ ΟΠΤΙΚΩΝ ΕΠΙΚΟΙΝΩΝΙΩΝ

# Σύστημα ανίχνευσης νεφών σε δορυφορικά δίκτυα

ΔΙΠΛΩΜΑΤΙΚΗ ΕΡΓΑΣΙΑ

# ΠΑΠΑΚΙΤΣΟΣ ΧΡΗΣΤΟΣ

Επιβλέπων: Φίλιππος Κωνσταντίνου
Καθηγητής Ε.Μ.Π.

Επιβλέποντες: Florian Moll, Martin Brechtelsbauer
Διπλωματούχοι Ηλεκτρολόγοι Μηχανικοί

Oberpfaffenhofen
Φεβρουάριος - Αύγουστος 2008

ΕΘΝΙΚΟ ΜΕΤΣΟΒΙΟ ΠΟΛΥΤΕΧΝΕΙΟ
ΣΧΟΛΗ ΗΛΕΚΤΡΟΛΟΓΩΝ ΜΗΧΑΝΙΚΩΝ
ΚΑΙ ΜΗΧΑΝΙΚΩΝ ΥΠΟΛΟΓΙΣΤΩΝ
ΤΟΜΕΑΣ ΣΥΣΤΗΜΑΤΩΝ ΜΕΤΑΔΟΣΗΣ ΠΛΗΡΟΦΟΡΙΑΣ ΚΑΙ
ΤΕΧΝΟΛΟΓΙΑΣ ΥΛΙΚΩΝ

DEUTCHES ZENTRUM FÜR LUFT- UND RAUMFAHRT
ΓΕΡΜΑΝΙΚΟ ΑΕΡΟΔΙΑΣΤΗΜΙΚΟ ΚΕΝΤΡΟ
ΙΝΣΤΙΤΟΥΤΟ ΕΠΙΚΟΙΝΩΝΙΩΝ ΚΑΙ ΠΛΟΗΓΗΣΗΣ
ΤΜΗΜΑ ΨΗΦΙΑΚΩΝ ΔΙΚΤΥΩΝ
ΟΜΑΔΑ ΟΠΤΙΚΩΝ ΕΠΙΚΟΙΝΩΝΙΩΝ

# Σύστημα ανίχνευσης νεφών
# σε δορυφορικά δίκτυα

ΔΙΠΛΩΜΑΤΙΚΗ ΕΡΓΑΣΙΑ

## ΠΑΠΑΚΙΤΣΟΣ ΧΡΗΣΤΟΣ

Επιβλέπων: Φίλιππος Κωνσταντίνου
          Καθηγητής Ε.Μ.Π.

Επιβλέποντες: Florian Moll, Martin Brechtelsbauer
          Διπλωματούχοι Ηλεκτρολόγοι Μηχανικοί

Εγκρίθηκε από την τριμελή εξεταστική επιτροπή την 8η Σεπτεμβρίου 2008

...........................    ...........................    ...........................
Φίλιππος Κωνσταντίνου    Νικόλαος Ουζούνογλου    Αθανάσιος Παναγόπουλος
Καθηγητής Ε.Μ.Π.    Καθηγητής Ε.Μ.Π.    Λέκτορας Ε.Μ.Π.

Oberpfaffenhofen
Φεβρουάριος - Αύγουστος 2008

....................................................

Χρήστος Γ. Παπακίτσος

Διπλωματούχος Ηλεκτρολόγος Μηχανικός και Μηχανικός Υπολογιστών Ε.Μ.Π.

# Acknowledgments

# Abstract

Clouds play an important role in regulating the radiation budget of the atmosphere and are responsible for altering or maintaining the global climate. Understanding the interaction between clouds and radiation is necessary for accurate models that predict future climate and weather changes. The present cloud instruments are imagers that operate in the visible spectrum, thereby operating only in the daytime. Other imaging instruments use completely different techniques for daytime and nighttime detection of clouds and have problems detecting clouds at sunrise and sunset.

The 'Cloud Detection System', a ground based, thermal infrared imager was developed to provide continuous 24-hour cloud measurement without difference in daytime or nighttime sensitivity. The system measures the down welling atmospheric radiance in the 7-14 μm region of the electromagnetic spectrum. The data collected are used to compute spatial and temporal cloud statistics.

Algorithms for processing the acquired data, for the cloud detection and for determining cloud statistics have been developed. From the analysis of the data, hourly cloud statistics show the trend of cloud coverage of the sky. Cloud distinguishing according to their thickness can be achieved by using various colorations of grey for the image analysis.

In this diploma thesis a system that performs sufficiently cloud detection was developed and the base for further research on this topic is set.

# Key words

cloud detection, cloud statistics, cloud thickness, IR imaging, thermal cloud radiation, hyperbolic mirror, image segmentation, angular resolution, spatial resolution, imager sensitivity

# Περίληψη

Τα σύννεφα παίζουν ένα σημαντικό ρόλο στη ρύθμιση της ακτινοβολίας από την ατμόσφαιρα και είναι υπεύθυνα για την αλλαγή ή την διατήρηση των κλιματικών συνθηκών. Η κατανόηση της αλληλεπίδρασης μεταξύ των νεφών και της ακτινοβολίας είναι απαραίτητη για ακριβή μοντέλα τα οποία προβλέπουν μελλοντικές κλιματικές και καιρικές αλλαγές. Τα υπάρχοντα όργανα για τα νέφη είναι απεικονιστές οι οποίοι λειτουργούν στο ορατό φάσμα ακτινοβολίας, για το λόγο αυτό λειτουργούν μόνο κατά τη διάρκεια της μέρας. Άλλα όργανα απεικόνισης χρησιμοποιούν διαφορετικές τεχνικές για ανίχνευση των νεφών τη μέρα και τη νύχτα και έχουν προβλήματα στην ανίχνευση κατά την ανατολή και τη δύση του ηλίου.

Το Σύστημα Ανίχνευσης Νεφών, ένας θερμικός απεικονιστής υπέρυθρης ακτινοβολίας τοποθετημένος στο έδαφος, αναπτύχθηκε για να παρέχει συνεχή 24-ωρη μέτρηση νεφών χωρίς διαφορά στην ευαισθησία του κατά τη διάρκεια της μέρας και της νύχτας. Το σύστημα μετράει την κατερχόμενη ατμοσφαιρική ακτινοβολία στη περιοχή 7-14 μm του ηλεκτρομαγνητικού φάσματος. Τα συλλεγόμενα δεδομένα χρησιμοποιούνται στον υπολογισμό χωρικών και χρονολογικών στατιστικών.

Έχουν αναπτυχθεί αλγόριθμοι για την επεξεργασία των ληφθέντων δεδομένων, την ανίχνευση νεφών και την δημιουργία στατιστικών. Από την ανάλυση των δεδομένων, ωριαία στατιστικά των νεφών δείχνουν την τάση της κάλυψης του ουρανού από τα νέφη. Η χρήση πολλών αποχρώσεων του γκρι στην ανάλυση των εικόνων οδηγεί στη διάκριση νεφών σύμφωνα με το πάχος τους.

Στα πλαίσια αυτής της διπλωματικής μελετήθηκε ένα σύστημα το οποίο ανιχνεύει επιτυχώς τα νέφη και τίθεται η βάση για μελλοντική έρευνα πάνω σε αυτό το θέμα.

## Λέξεις κλειδιά

ανίχνευση νεφών, στατιστικά νεφών, πάχος νεφών, υπέρυθρη απεικόνιση, θερμική εκπομπή νεφών, υπερβολικός καθρέφτης, μερισμός εικόνας, γωνιακή ανάλυση, χωρική ανάλυση, ευαισθησία απεικονιστή

# Contents

# Figures

# Tables

# CHAPTER 1

# Introduction

## 1. 1   Purpose of the Thesis

The purpose of the thesis is the development and test of a Cloud Detection System with hemispherical observation. The main goal of the system is to determine if there is a link blockage by clouds in an optical downlink or uplink from satellites, HAPS and UAV. A network of ground stations can be developed and, in case of cloud blockage, the signal can be transmitted through a station placed in an area with clear sky. Another implementation of the system is the definition of the current cloud coverage at various geographical positions and the collection of meteorological statistics. Note that the system is operational 24 hours per day due to the usage of the Photon Camera which works at the middle infrared region of the electromagnetic spectrum.

## 1. 2   Abstract of the Thesis

The thesis is divided into three main parts. In the first part, there is an introduction to the physical characteristics of clouds in order to understand the theory on which the Cloud Detection System is based. The second part is dedicated to the description of the system structure and important technical issues. Finally, the third part contains the software and the results of the image analysis.

***Chapter 1*:** In chapter one, there is an introduction of the thesis with its purpose and goals.

***Chapter 2*:** The second chapter contains information about the different types of clouds, their physical characteristics and the radiation emitted from cloudy and clear sky. Moreover, there is an example of calculated radiation from clouds.

***Chapter 3*:** In the third part the alternative structures of the Cloud Detection System are presented with their dimensions, technical information, advantages and weaknesses. In the end, the most appropriate structure is chosen.

***Chapter 4*:** This chapter analyzes the components of the chosen structure. Data about the mirror, the Photon Camera, the system's geometry and photographs belong to this part of the thesis.

***Chapter 5*:** This chapter provides important information about the performance of the system. The angular and the spatial resolution as such the interferences are studied. These parameters define in a sufficient way the system's performance.

***Chapter 6*:** This chapter contains the software programs developed in the thesis. There are the flowcharts of the grabbing and the segmentation program and an explanation of the used algorithm.

***Chapter 7*:** In this chapter, there are the results of the thesis. It contains the improvement methods used in the analysis, such as special masks and filters. Moreover, a method of distinguishing thin and thick clouds is presented. There is a chronological analysis of the cloud coverage of the sky. Finally, there is a reference to critical cases, such as clear or overcast sky and the presence of the sun.

***Chapter 8*:** The last chapter is the conclusion of the thesis. There are presented the general results of the thesis and the future steps of research on this topic are set.

<div align="right">**CHAPTER 2**</div>

# Physical Characteristics and Radiation of Clouds

## 2. 1  Introduction

Clouds always capture the interest due to their wide variety of shapes, sizes, and colors, and for their unpredictable and complex nature. They form when the dew point of water is reached in the presence of condensation nuclei in the troposphere. Atmosphere is a dynamic system, and the local conditions of turbulence, uplift and other parameters give rise to many types of clouds. Various types of clouds occur frequently enough to have acquired a name of their own; often these are further specified with additional descriptive name. Furthermore, various atmospheric processes can make the clouds organize in distinct patterns such as 'wave cloud' or 'actinoform cloud', which are large scale structures and not always readily identifiable from a single point of view. The primary constituent of clouds is a conglomeration of water and/or ice growing on small particles called condensation nuclei. These tiny particles are mostly hygroscopic, vary in size, and are produced from many sources like volcanoes, smokestack, and atmospheric chemical reactions. [Zis96]

## 2. 2  Cloud Types

Clouds are classified primarily according to their size, shape, constitute and their altitude above the ground level. There are two general categories regarding the shape of clouds: layered and convective. The first category is called stratus clouds (from the Latin stratus that means 'layer') and the second cumulus clouds (from the Latin cumulus that means 'piled up').  Moreover, there is a system, proposed by Luke Howard in 1802, which classifies the cloud by their base height. According to this system the clouds are divided in the following four families (see *Figure2.1* for the illustrated description):

- Family A: developed above 22,000 ft and denoted by the prefix *cirro-*.
- Family B: developed between 14,000-22,000 ft and denoted by the prefix *alto-*.
- Family C: developed lower than 14,000 ft. When the clouds contact the ground, they are called 'fog'.
- Family D: vertical clouds. They form at many heights. [Kar88]
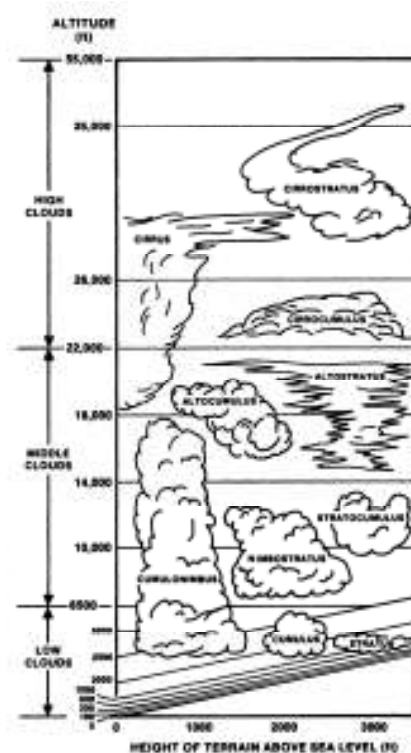


**Figure 2. 1**  Cloud classification by altitude of occurrence [Kar88].

Another classification introduced by the World Meteorological Organization [Wmo08] divides the clouds in ten different types. *Table 2.1* summarizes the main features of these types and in *Figure2.2* there are pictures of them.

| Cloud Type | Abbrev. | Symbol | Family | Altitude $h_c$ (m) | Appearance |
|---|---|---|---|---|---|
| Altocumulus | Ac | ⋈ | B | 2400-6100 | large and dark patched clouds |
| Altostratus | As | ∠ | B | 2000-5000 | sheet or layer, can usually see the sun through it |
| Cirrocumulus | Cc | - | A | > 6000 | small, high, patched clouds, in rows |
| Cirrostratus | Cs | - | A | > 6000 | white veil |
| Cirrus | Ci | - | A | > 7000 | thin, wisplike strands |
| Cumulonimbus | Cb | - | D | 2000-16,000 | very tall and large clouds |
| Cumulus | Cu | - | C | < 2000 | like rising mounts |
| Nimbostratus | Ns | ⬰ | C | < 2400 | dark, widespread, formless layer |
| Stratocumulus | Sc | - | C | < 2400 | large dark, rounded masses, in groups, lines, or waves |
| Stratus | St | — | C | < 2000 | horizontal layers |

**Table 2. 1**   Cloud types and properties [Wmo08].

These ten cloud categories have subdivisions like wave clouds, which look like lens with sharp edges, and noctilucent clouds, which are located in the mesosphere at altitudes of around 75 ~ 85 km and were composed of volcanic or meteoric dust, but they are now known to be primarily composed of water ice.

The prefix *Nimbo-* and the suffix *–nimbus* refer to clouds that produce precipitation. Cumulonimbus and nimbostratus clouds cause intense precipitation. Cumulus clouds are sometimes called fair weather clouds but can develop into more storm-condition clouds (cumulonimbus, for example), and continued upward growth suggests showers later in the day. Other precipitation clouds are the altostratus, the cirrocumulus and the stratus but the last one in a minor grade. Isolated cirrus clouds often indicate a stable situation and do not bring precipitation. However, large amounts of cirrus clouds can indicate an approaching storm system. Stratocumulus clouds bring only light rain or snow. These clouds are often seen at either the front or tail end of worse weather and may indicate storms to come, in the form of thunderheads or gusty winds. On the other hand, altocumulus and cirrostratus clouds are no precipitation clouds. [Wmo08]



**Figure 2. 2**   Appearance of different cloud types [Aus08].

## 2. 3   Physical Characteristics of Clouds

Many physical characteristics of clouds, in particular the cloud phase synthesis and the water content, are temperature dependent, and it is precisely this dependency which frequently determines the seasonal and latitude variations of the physical parameters. The *Table2.2* contains the mean cloud temperature for different altitudes. The temperature of the surrounding air differs by some tenths of a degree from the cloud temperature. Convective clouds tend to heat up the surrounding atmosphere somewhat. Within the cloud mass itself, however, the

temperature fluctuations may be considerable, reaching 1 to $3^{\circ}$ C. On the average, these clouds stay a little $(0.2 - 0.5^{\circ}$ C) cooler than the ambient air.

| Cloud Altitude $h_c$ (km) | Mean temperature T ($^{\circ}$ Celsius) |
|---|---|
| 0.00 | 15 |
| 1.25 | 8 |
| 2.50 | -1 |
| 3.75 | -6 |
| 5.00 | -13 |
| 6.25 | -24 |
| 7.50 | -34 |
| 8.75 | -41 |
| 10.00 | -50 |
| 11.25 | -57 |

Table 2. 2   Temperature of clouds [Gma07].

As it is mentioned, the cloud phase is determined by the temperature. *Table 2.3* gives the mean frequencies of the various phases at various temperatures for clouds of all forms. These data are practically independent of the season of the year.

| Phase of cloud | Temperature (from-to), °C | | | | | | | | | | | |
|---|---|---|---|---|---|---|---|---|---|---|---|---|
| | 0 −2 | −4 −6 | −8 −10 | −12 −14 | −16 −18 | −20 −22 | −24 −26 | −28 −30 | −32 −34 | −36 −38 | −40 −42 | −44 −46 |
| Droplet | 84 | 69 | 54 | 37 | 23 | 17 | 10 | 6 | 3 | 2 | 1 | 0 |
| Mixed | 14 | 26 | 35 | 42 | 40 | 35 | 31 | 25 | 17 | 11 | 7 | 6 |
| Crystal | 2 | 5 | 11 | 21 | 37 | 48 | 59 | 69 | 80 | 87 | 92 | 94 |

Table 2. 3   Frequencies (%) of different phases of clouds as function of temperature [Fei84].

The mixed phase cloud contains both droplets and crystals. The concentration of ice nuclei, which determines the probability of the appearance of crystals in the cloud, increases sharply with a decrease in temperature. The smaller the droplets, the more likely it is that unfrozen droplets will be present in the cloud at the given temperature. Finally, important role in the cloud phase

plays the seeding of lower-lying layers with crystals falling from higher layers at a lower temperature.

In clouds, as a rule, the moisture content is close to saturation. Consequently, the amount of water in vapor form is determined solely by the temperature. The absolute saturation moisture content *decreases* sharply with a drop in temperature, as is evident from *Table 2.4* which shows the temperature dependence of absolute saturation moisture content *a*. The dimension of *a* is $g/m^3$ or $g/cm^3$ and is referred to the mass per unit cloud volume.

| t ($^oC$) | 20 | 10 | 0 | -10 | -20 | -30 |
|---|---|---|---|---|---|---|
| $a_w$ (g/m$^3$) | 17.6 | 9.7 | 4.8 | 2.3 | 1.0 | 0.45 |
| $a_i$ (g/m$^3$) | - | - | 4.8 | 2.15 | 0.88 | 0.34 |

**Table 2. 4** Temperature dependence of absolute saturation moisture content *a* ($a_w$ = saturation with respect to water; $a_i$ = saturation with respect to ice) [Fei84].

In vertically extensive clouds the mean water content $\overline{w}$ over the cloud section increases with the distance from the ground base, reaching the highest value $\overline{w}_{max}$ in the upper part of the cloud (at a height of about $0.8H_c$, where geometrical thickness of the cloud). The values $\overline{w}_{max}$ depend on the cloud thickness and on the temperature. *Figure 2.3* contains values of $\overline{w}_{max}$ for various cases of cloud thickness and temperature $t_{lb}$ on cloud base.
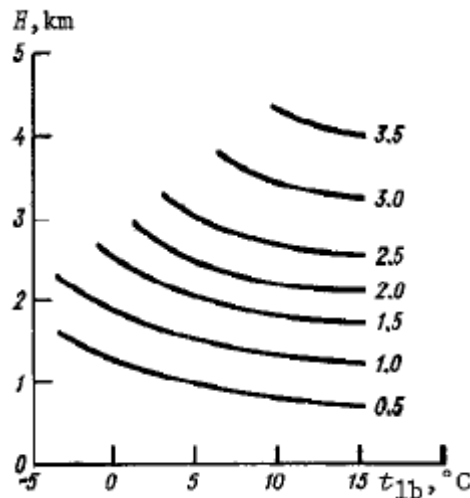


**Figure 2. 3** Dependence of $\overline{w}_{max}$ on cloud thickness and temperature $t_{lb}$ on cloud base. Numbers by curves indicate values $\overline{w}_{max}$ of in g/m$^3$ [Fei84].

The concentration and size of cloud droplets can vary greatly, but if averages over large volumes of cloud and over many cases are considered then definite regularities show up in the droplet-size distributions. The radii of most cloud droplets range from a few microns to some tens of microns. The droplet concentration varies from tens per $cm^3$ to thousands per $cm^3$. The concentration of large droplets (radii greater than 100 μm) is usually 1/1000 to 1/10,000, being 0.1-10 per liter. In the presence of precipitation, the rain drop concentration (radii greater than 100-200 μm) may be 10-100 per liter. Along with cloud droplets, clouds also contain water-coated condensation nuclei; these take the form of tiny droplets about 1 μm or less in radius which are in equilibrium with the cloud material. Since in a cloud the moisture content is close to 100%, the radii of these droplets are 5 to 10 times the radii of the nuclei dissolved in them. On the whole, the averaged distributions (size spectra) of the droplets in a cloud have the form shown in *Figure 2.4*. In clouds of the middle latitudes $r_{c,min}$ usually ranges from 0.5 to 2.0 μm, and $r_{c,mod}$ (mode radius) from 2.5 to 7 μm.
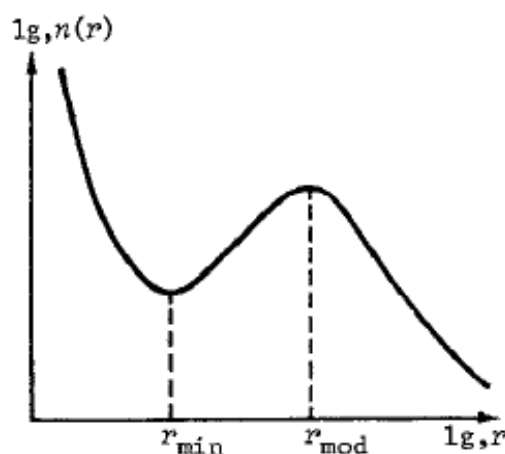


**Figure 2. 4** Density of droplet-size distribution [Fei84].

In contrast to the case with droplets, when considering crystals in clouds it is important to know their shape and orientation as well as their size and number. Ice particles in clouds can be divided into three groups, according to shape: rounded, laminar, and acicular. The first group includes particles whose dimensions in any direction are about the same; the second and third groups include particles which are appreciably smaller in one direction than in a perpendicular direction. The shape of the cloud crystals depends on the

temperature and the humidity. Since, when crystals originate in clouds, the humidity is close to the saturation value of water, the shape of a crystal being formed may, as a first approximation, be related only to the temperature. The sizes of the crystals in clouds are usually hundreds of microns along the major axis, with plate or column (needle) thickness of ten of microns. The ice content that is, the mass of ice in the crystals, range from $10^{-3}$ g/m$^3$ in high-level clouds to $10^{-1}$ g/m$^3$ in St and Ns. The concentration ranges from some units or tens per liter in high-level clouds to tens or hundreds per liter in Ns, As systems.

Finally, *Table 2.5* shows important parameters for chosen types of clouds: altitude $h_c$, geometrical thickness $H_c$, concentration $N_c$, mean cloud-droplet size $r_c$ and mean water content $\overline{w}$. [Fei84]

| Cloud Type | $h_c$ (km) | $H_c$ (km) | $N_c$ (cm$^{-3}$) | $r_c$ (μm) | $\overline{w}$ (g/m$^3$) |
|---|---|---|---|---|---|
| Ac | 4.8 | 0.2 | 90 | 8 | 0.2 |
| St | 1.0 | 0.45 | 220 | 8 | 0.4 |
| St | 1.0 | 0.4 | 100 | 10 | 0.4 |
| St | 0.4 | 0.15 | 70 | 8 | 0.13 |
| Cs | 8.4 | 1.5 | - | - | - |

**Table 2. 5** Microphysicals and macrophysicals parameters of clouds, according to measurements made in April 1971 over Black Sea (Sun height h = 52$^o$, for Cs h = 48$^o$) [Fei84].

## 2. 4  Clear Sky and Cloud Radiation

There are two significant phenomena that cause the sky infrared background radiation. The first is the emission from atmospheric constituents and the second the scattering of the sun's radiation. The two types of radiation are located in different regions in the electromagnetic spectrum. The solar scattering region is until 3 μm and the thermal emission region beyond 4 μm. *Figure2.5* illustrates the contributions from scattering and atmospheric emission to blackbody radiation. Solar scattering is represented by reflection from a bright sunlit cloud and also by a curve for clear-air scattering.

The radiation in *Figure 2.5* is also illustrated by blackbodies in specific temperatures. It is assumed that the sun's temperature is 6000 K and the emission of atmospheric constituents is equal to a blackbody in 300 K. This is only an approximation of the real situation.
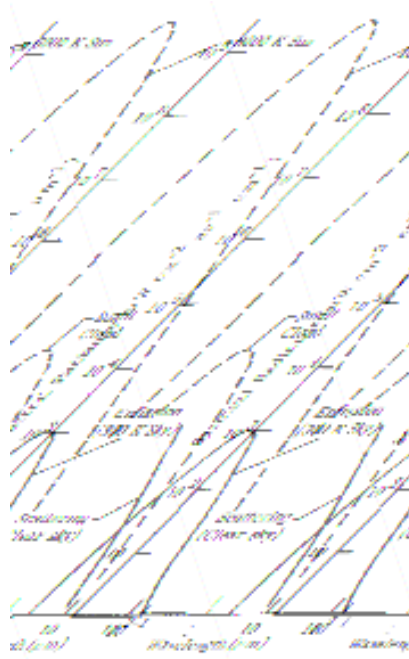


**Figure 2. 5** Contributions from scattering and atmospheric emission to blackbody radiation [Zis96].

According to the Planck's law [Zis96], a black body (an object that absorbs all light that falls on it) at temperature *T* emits electromagnetic radiation at all wavelengths. The spectral radiance *I* comes out from the following equation as a function of wavelength $\lambda$:

$$I(\lambda, T) = \frac{2hc^2}{\lambda^5} \frac{1}{e^{\frac{hc}{\lambda \kappa T}} - 1} \quad [\text{J} \cdot \text{s}^{-1} \cdot \text{m}^{-2} \cdot \text{sr}^{-1} \cdot \text{m}^{-1}] \tag{2. 1}$$

where  *h* is Planck's constant, 6.6262 * 10^-34 [Js]

$\quad$ *c* is the velocity of light in vacuum, 2.9979 * 10^8 [m/s]

$\quad$ $\lambda$ is the wavelength [m]

$\quad$ *k* is Boltzmann's constant, 1.3806 * 10^-23 [J/K]

$\quad$ *T* is absolute temperature in Kelvin [K]

This simple model is modified by a number of factors. Regarding the solar scattering region, there are absorption bands that reduce the radiation. Earth atmosphere has the so called IR Atmospheric Windows. Atmosphere is transparent only in a few narrow wavelength ranges due to absorbing bands of atmospheric particles. Water vapors absorb the sun radiation at 0.94, 1.1, 1.4, 1.9 and 2.7 μm while the carbon dioxide absorb at 2.7 μm. *Figure 2.6* shows the spectral radiance of a clear sky during the day. There is a decrease of the radiation in the bands of absorption.

*Figure2.7* describes the spectral radiance of a clear sky for two cases of sun elevation (15° and 77°). The observation angle is 90°. When the sun elevation is near the zenith the collected radiation increases.
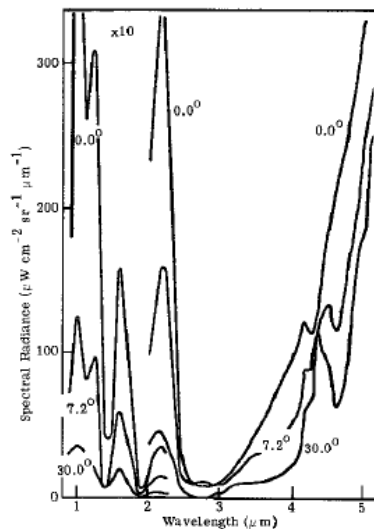


**Figure 2. 6**  The spectral radiance of a clear daytime sky [Zis96].
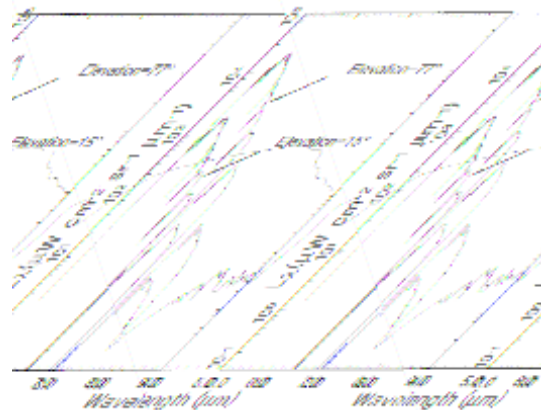


**Figure 2. 7**  The spectral radiance of a clear sky as a function of sun elevation calculated by LOWTRAN 7 [Zis96].

Another parameter that affects the solar scattering radiation is the presence of clouds in the atmosphere. The cloudier the sky is more sun radiation is blocked.

On the other hand, those bands of solar region with strong absorption are replaced in thermal region with bands with strong emission. The curves of these bands approach the blackbody curve appropriate to the temperature of the atmosphere. Measurements of the spectral radiance of a clear nighttime sky for several viewing angles taken from a high, dry location show this relationship in *Figure 2.8*. There is a strong band of $CO_2$ at 15 μm and of $H_2O$ at 6.3 μm. These

bands are also responsible for the low-level continuum. There is also a weak emission peak at 9.6 µm due to the radiation from ozone. Humidity affects the thermal radiation. *Figure 2.9* shows measurements of the spectral radiance of a clear nighttime sky for various angles of elevation above the horizon taken at a humid sea-level location. The comparison of the radiation in the same viewing angle of *Figure 2.8* and *Figure 2.9* indicates that moist atmosphere emits more radiation due to the increased presence of water vapors. The radiation decreases when the elevation angle increases at the same altitude. The reason is that when the elevation angle increases, the observed area of the sky reduces considering the same altitude so the amount of emitting atmospheric particles decreases.
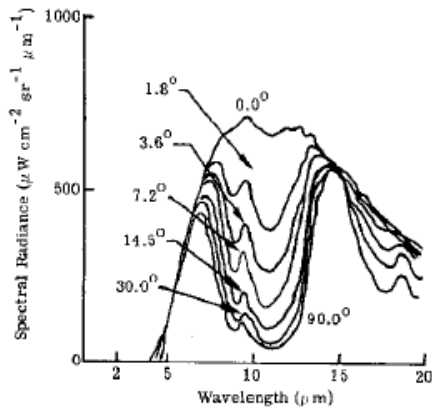


**Figure 2. 8**  The spectral radiance of a clear nighttime sky. It is for several angles of elevation above the horizon (Elk Park Station, Colorado) [Zis96].
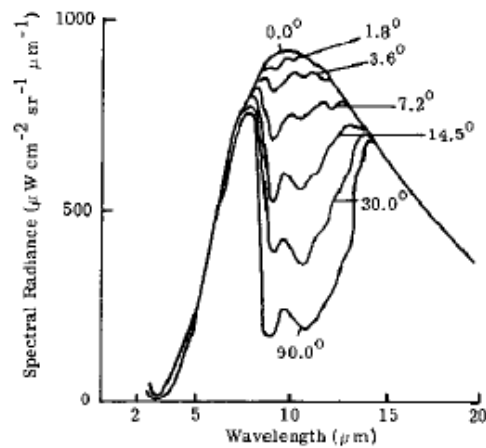
**Figure 2. 9**  The spectral radiance of a clear nighttime sky. It is for several angles of elevation above the horizon (Cocoa Beach, Florida) [Zis96].

The elevation angle of the sun has little effect on the thermal region but the temperature of the atmosphere affects strongly this kind of radiation.

Not only the atmosphere constituents, but also clouds emit radiation. Thick clouds are considered as good blackbodies. Their emission band is 8- to 13-µm. The temperature of the cloud determines the radiation.

The strong absorption and emission bands of the atmosphere at 6.3 and 15.0 µm may cause detection problems. A striking example is given at the *Figure 2.10*. It shows the spectral radiance of the underside of a dark cumulus cloud. In these regions the radiation is determined by the temperature of the atmosphere. To

be more specific, the atmospheric temperature at the ground level is $+10^o$ C and the radiation at 6.3 and 15.0 μm approaches that of a blackbody at this temperature. In the region of 8-13 μm, the radiation looks like that of a blackbody at the temperature of the underside of a cloud, which means $-10^o$ C. This distortion of the radiation spectrum may make clouds invisible in these regions.
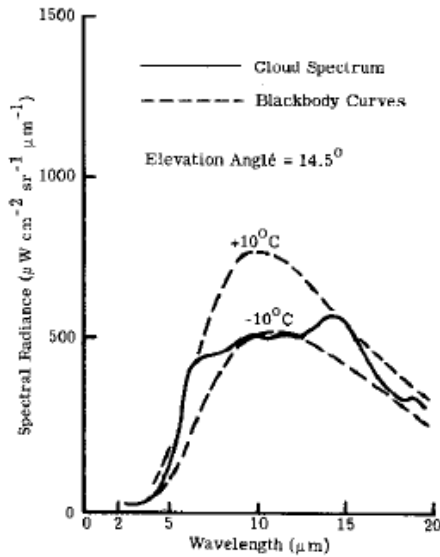


**Figure 2. 10** The spectral radiance of the underside of a dark cumulus cloud [Zis96].
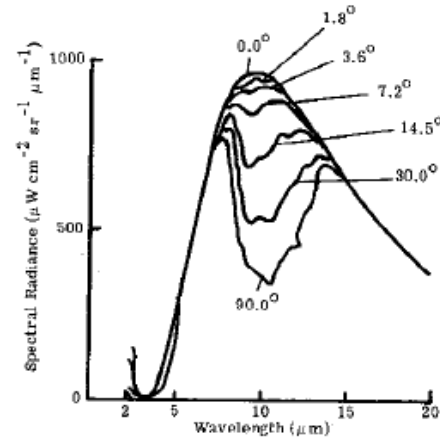


**Figure 2. 11** The spectral radiance of sky covered with cirrus clouds at several angles of elevation [Zis96].
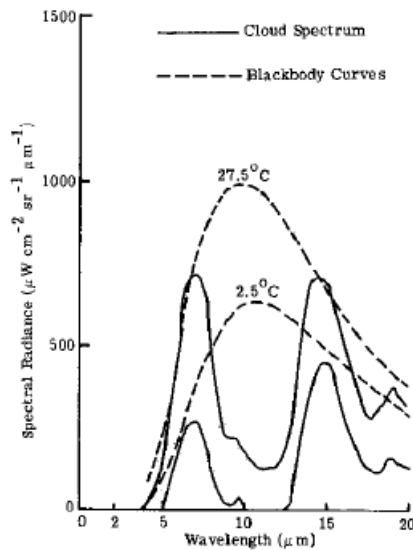


**Figure 2. 12** Zenith sky spectral radiance showing the large variation with ambient air temperature [Zis96].
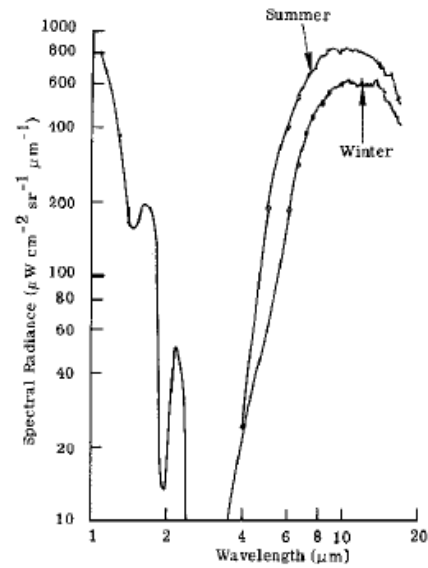


**Figure 2. 13** Spectral radiance of overcast skies in winter and summer [Zis96].

*Figure 2.11* illustrates the spectral radiance of a sky with cirrus clouds for several angles of observation. Likewise for the atmospheric particles, the radiation, not only from cirrus clouds but also from all cloud types, is reduced when the angle increases for the same reasons. The *Figure 2.12* and *Figure 2.13* show the spectral radiance for several ambient air temperatures indicating the dependence of the radiation on the cloud environment. [Zis96]

The cloud radiation is depended on the geometric thickness of the cloud and the ice concentration $w_i$. *Figure 2.14* illustrates the radiance for different situations and wave numbers $v$. The wave number $v$ is defined as $v = 1/\lambda$ with unit m$^{-1}$. When the ice concentration increases, the radiation also increases. The reason is the presence of more emitting particles. The radiation decreases while the values of wave number $v$ increase and increases with the thickness for a specific range of values. At large ice concentrations there is a peak at small thicknesses followed by a gradual decrease in the radiance for larger thicknesses. Again at even larger thicknesses, the radiance increases.

This variation in the radiance can be explained by the fact that there is a competition of two opposing tendencies. As the thickness of the cloud layer is increased there is a tendency for the radiance to increase because of the larger radiating mass. However, the transmission through the cloud layer tends to decrease with increasing thickness, thereby attenuating the radiation as it passes through the remainder of the cloud from its source area. For small cloud thicknesses the transmissivity does not change sufficiently fast to overcome the increase in the radiance due to the increase in the radiating mass. At larger thicknesses the decrease in transmissivity begins to dominate, resulting in a decrease in the radiance. Again, at very large thicknesses the transmissivity does not decrease very fast while the radiating mass continues to increase. There is then a slight increase in the radiance at this point. Also shown in the figure by the dashed curves are the blackbody radiances corresponding to the temperature of the cloud tops. A radiance greater than the blackbody value means only that radiation from warmer lower layers is transmitted through  the cloud with a resulting radiance that is greater than that which could be emitted by a blackbody at the colder cloud top temperature. [Jac70]
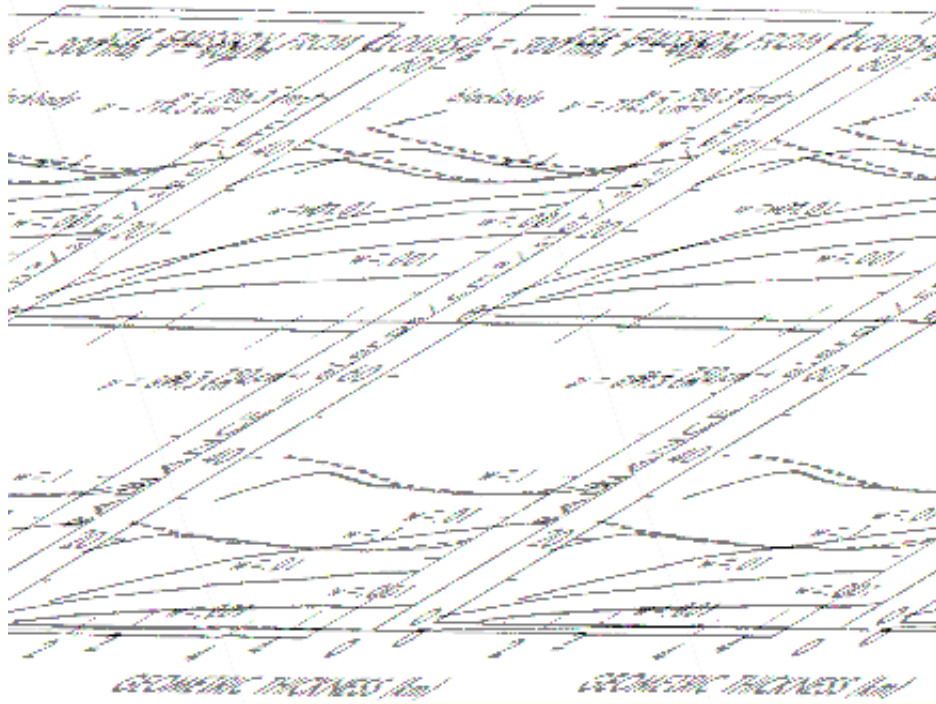
**Figure 2. 14** Radiance due to the self-emission from the cloud versus the geometric cloud thickness. $w$ is the ice concentration in the units, $g/m^3$. The dashed curves are the blackbodies curves [Jac70].

## 2. 5  Calculated Cloud Radiation

An approximate calculation of the cloud radiation can be achieved using the *equation 2.1* of Plank's law for blackbodies and the relevant theory. *Figure 2.15* illustrates the plot of the scenario used for the calculations. Clouds are at the altitude of 2 km above the ground level and their temperature is $0^o$. Clouds radiate like a blackbody and there is no attenuation due to the atmosphere and the way to the ground. The Photon Camera is marked with its image plane. The assumed mirror has the hyperbolic shape described in *equation 4.7*. The calculated radiation is the radiation that is collected by every pixel of the MIR camera. So, the mirror area $dS$ that covers one pixel and the corresponding solid angle for this area $dv$ are multiplied with the incident thermal radiance. The distance $r$ is the distance of the area $dS$ from the center of the mirror.
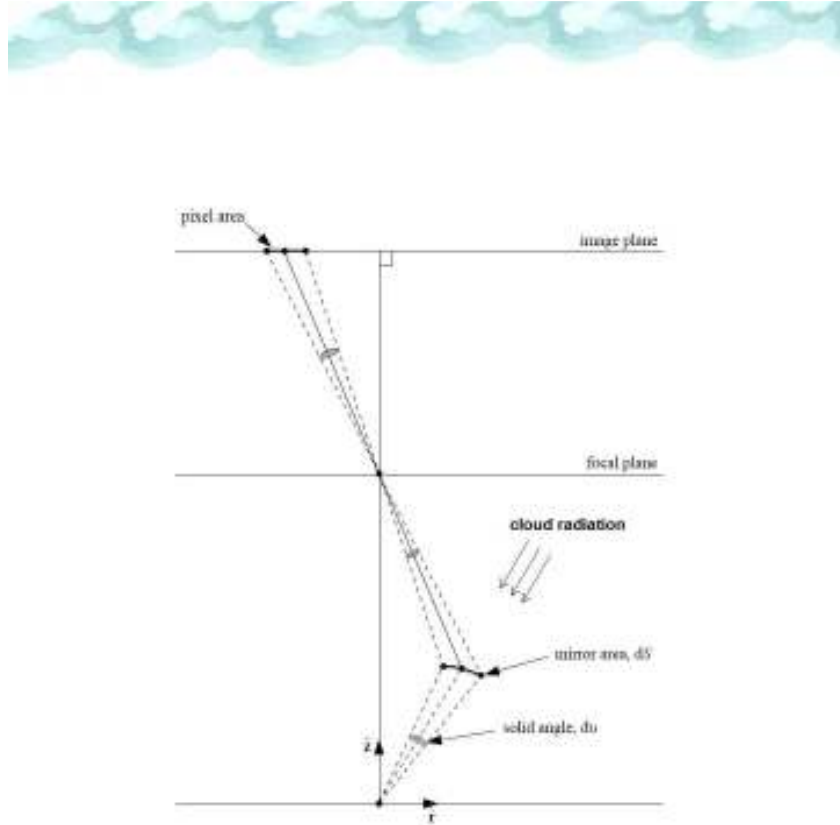
**Figure 2. 15**   Plot of the system [Bak99].

The radiation is calculated for the right part of the mirror. The radiation curve of the left part has the corresponding form. The first step is to calculate the cloud radiation. *Equation 2.1* gives the radiation curve as a function of the wavelength at the range of 7-14 μm. The integration of this curve concludes to the value 814.66 w/m$^2$/sr which is the collected radiation from the operating spectrum of the Photon Camera. The solid angle of every pixel *dv* and the mirror area *dS* that covers one pixel are calculated according to the method of *paragraph 5.2.1*. The multiplication of *dS* and *dv* with the total cloud radiance (814.66 w/m$^2$/sr) leads to the collected radiation for every single pixel of the Photon Camera. *Figure 2.16* illustrates the thermal cloud radiation as a function of distance *r* from the centre. The radiation reduces at the edges of the mirror and the highest value is at the center. This is the result of two opposite trends described at *paragraph 5.2.1*. The solid angle of every pixel *dv* reduces rapidly from the central to the boundary pixels. On the other hand, the area of every pixel on the mirror *dS* increases from the centre to the edges. The first trend is more intense and so the final radiation is less at the edges.
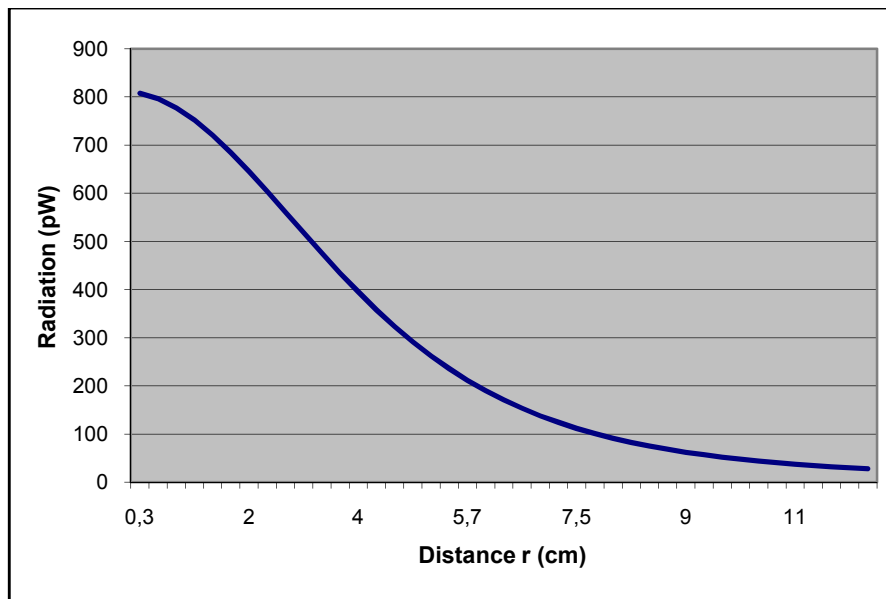
**Figure 2. 16**  Thermal cloud radiation for every pixel of the MIR camera.

# CHAPTER 3

# Proposed Structures of the Cloud Detection System

## 3. 1   Introduction

This chapter evaluates the different proposals for the catadioptric system and concludes to the most appropriate choice. A catadioptric system is a combination of lenses and mirrors placed in a carefully arranged configuration in order to adjust the field of view to system's purposes [Bak99]. The constructing aim is to cover $160^{o}$ of the hemisphere with the FoV of the system. There is no interest in capturing the angle of $10^{o}$ from the ground because there are many obstacles such as human constructions, trees, hills etc. So the total angle of $20^{o}$ ($10^{o}$ from each side of horizon) can be omitted and take into account the rest $160^{o}$. As the field of view (FoV) of the Photon Camera is quite small, the camera itself could not cover such a big area without using an additional mirror or lens.

The critical parameter for the size of the system is the total FoV of $160^{o}$. This means that the boundary beam of the small FoV of the Photon Camera, when it is reflected on a mirror, should have $10^{o}$ elevation from the ground. Note that there are four available versions of the Photon Camera with different values of FoV. *Table 3.1* gives the relevant information. The calculations below were made for each version.

| Name | Abbreviation | Field of View |
|------|--------------|---------------|
| Camera 1 | C1 | 50º x 38º |
| Camera 2 | C2 | 36º x 27º |
| Camera 3 | C3 | 20º x 15º |
| Camera 4 | C4 | 14º x 11º |

**Table 3. 1** Versions of the Photon Camera [Fli08].

# 3. 2 The proposed structures

Many ideas were proposed for the structure of the catadioptric system. Among them, four are considered to be applicable. They are presented below separately with details for the dimensions.

## 3. 2. 1 System I

The *Figure 3.1* presents the structure of System I. The system contains a box and the Photon Camera is placed at the bottom of it, pointing vertically. At the upper part of the box, in the middle, is placed a lens (light green line).
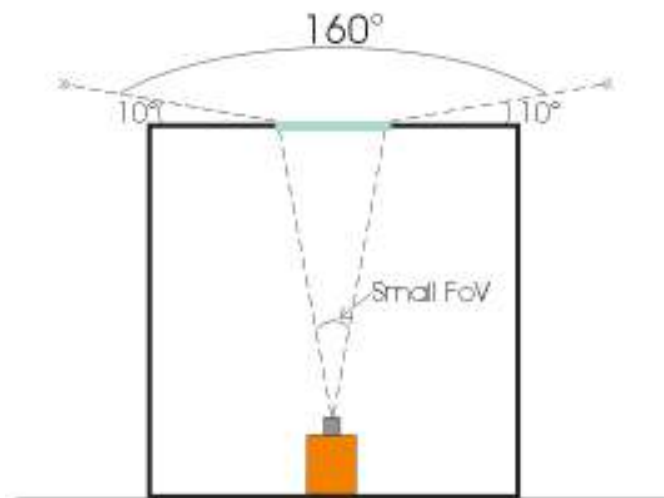


**Figure 3. 1** Plot of System I.

The box is responsible for the weather protection of the camera, since the system is used outside. The material should be resistant to bad weather conditions. A good proposal is the use of aluminum as such it is almost completely resistant to corrosion due to its natural oxide that is developed when it is exposed to air. Moreover, it is extremely durable.

The lens is used for two reasons. First of all it is used to broaden the FoV of the camera until the value of $160^o$. So, a lens with the appropriate focal length should be selected. The lens should be convex. The second use of the lens is to protect the camera from weather conditions in combination with the box. So, it should be waterproof. The lens must be almost transparent to the electromagnetic range of 8-14 μm, the range that used to capture images from the sky. The following alternative solutions could be implemented in System I:

- Silicon: the transmission curve shown in *Figure 3.2* depicts the typical transmission for a 1 mm thick piece of uncoated silicon as a function of wavelength.
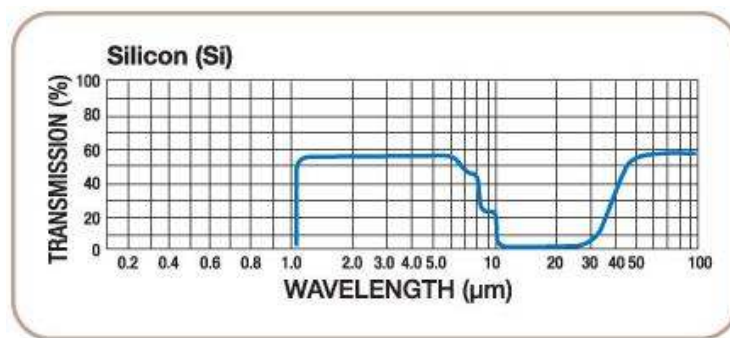


**Figure 3. 2**   Transmission curve of Silicon [Tho08].

- Germanium: the transmission curve shown in *Figure 3.3* depicts the typical transmission for a 2 mm thick piece of uncoated germanium as a function of wavelength.
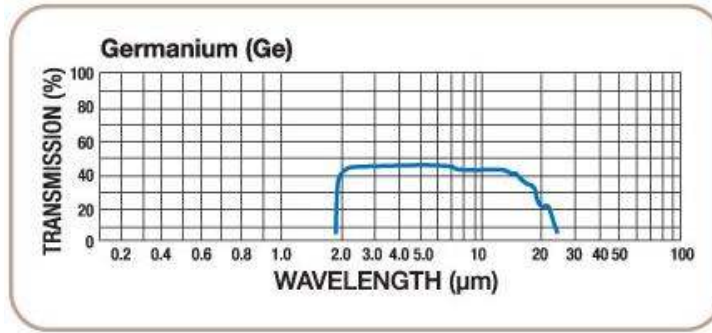
**Figure 3. 3** Transmission curve of Germanium [Tho08].

- Zinc Selenide: the transmission curve shown in *Figure 3.4* depicts the typical transmission for a 1 mm thick piece of uncoated Zinc Selenide as a function of wavelength.
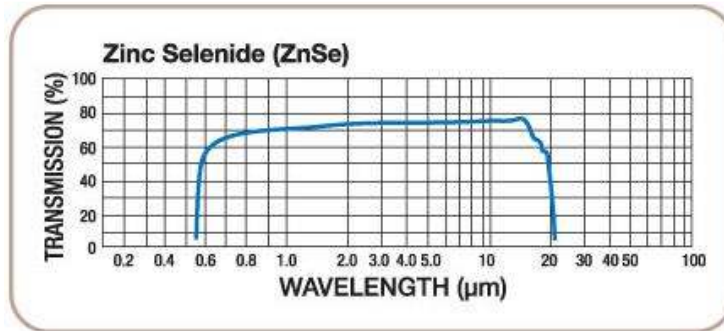


**Figure 3. 4** Transmission curve of Zinc Selenide [Tho08].

ZnSe is the most appropriate material for the Cloud Detection System as it is more transparent to middle infrared radiation and for a wider range of the electromagnetic spectrum.

The small FoV should cover the whole lens. So, the dimensions of the system are depended on the value of FoV. Taking into account that a usual lens has diameter 25.4 mm, the distance d between the camera and the lens is calculated from the following formula:

$$d = \frac{12.7}{\tan(\frac{smallFoV}{2})} \qquad (3.1)$$

The results are shown in *Table 3.2*.

| | C1 | C2 | C3 | C4 |
|---|---|---|---|---|
| **d (mm)** | 36.9 | 52.9 | 96.5 | 131.9 |

**Table 3. 2**   Values of distance D of System I.

The smaller the FoV or the bigger the focal length is, the bigger distance $d$ is needed.

## 3. 2. 2   System II

*Figure 3.5* and *Figure3.6* show the possible structures of the system. The difference is only the shape of the mirror. System II can be implemented with a convex mirror or a concave one. The Photon Camera points at the mirror horizontally. It is protected from the weather conditions by a metallic housing. It should not be very long because it might block the radiance to fall on the mirror. What is more, there is no need in using the whole mirror but only a part of it. The beams are reflected in a way so that the total FoV of these systems is $160^{\circ}$.
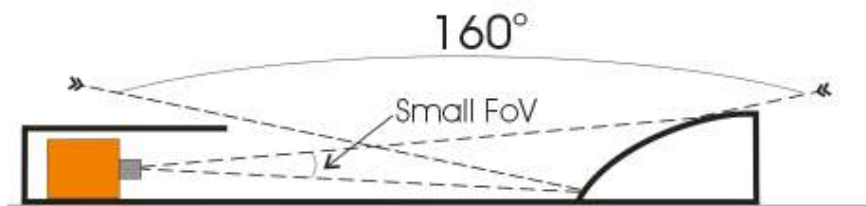


**Figure 3. 5**   First version of System II.
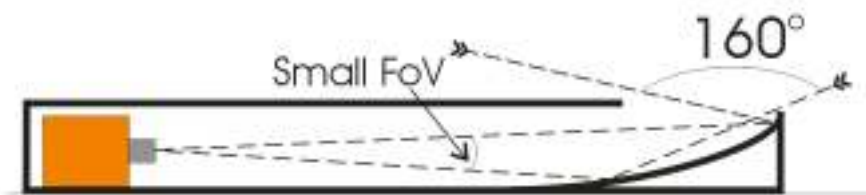


**Figure 3. 6**   Second version of System II.

To have a better overview of the systems, arithmetical examples where done for the first version of System II. *Figure 3.7* describes the parameter *u* that was calculated. The mirror is considered as a sphere with radius *r*.
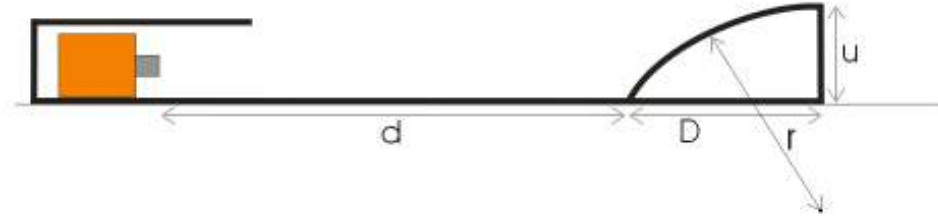


**Figure 3. 7**   Calculated dimensions of System II.

Parameter *u* of each version of the Photon Camera is calculated approximately from the following equation:

$$\tan(\frac{smallFoV}{2}) = \frac{u/2}{d} \Rightarrow u = 2d\,\tan(\frac{smallFoV}{2}) \qquad (3.\,2)$$

*Table 3.3* contains the relevant arithmetical results. Notice that the small FoV should cover almost the whole part of the mirror.

| d (cm) | u (cm) | | | |
|---|---|---|---|---|
| | C1 | C2 | C3 | C4 |
| 40 | 27.2 | 19.2 | 10.4 | 7.6 |
| 60 | 40.8 | 28.8 | 15.6 | 11.4 |
| 80 | 54.4 | 38.4 | 20.8 | 15.2 |

**Table 3. 3**   Values of dimension u for different cases.

It is important to take into account that the previous values of *u* are a good approximation of the real values, which are a bit bigger. This happens, firstly, because the small FoV of the camera does not cover exactly the whole part of the mirror but a slightly smaller part and for the evaluation of the parameter *u* this part is used. Secondly, the distance *D* is not taken into account in order to simplify the calculations. The parameter *u* increases while the parameter *d* increases and the camera has bigger FoV.

## 3. 2. 3   System III

Another suggestion for the Cloud Detection System is illustrated at the *Figure 3.8*.
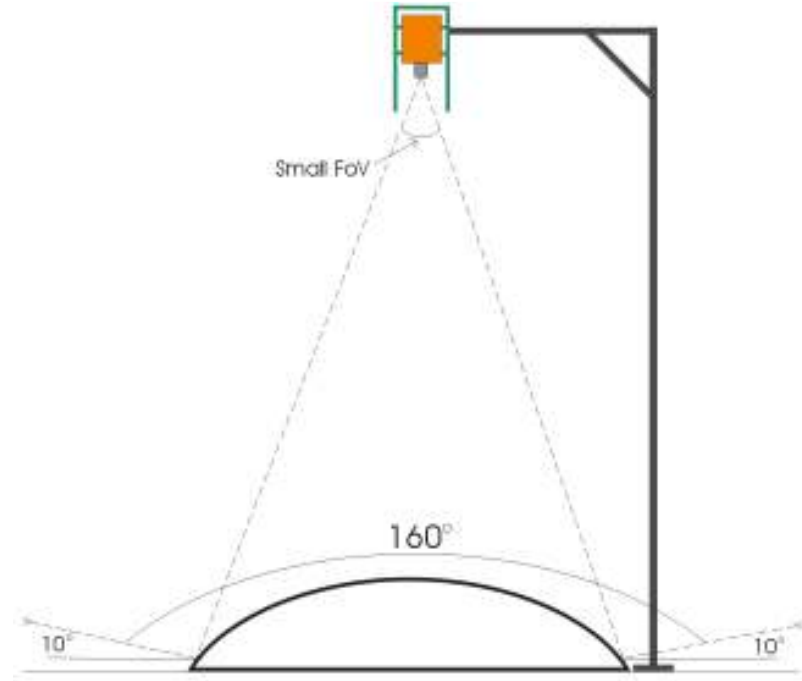


**Figure 3. 8**   Plot of System III.

The system consists of a spherical convex mirror placed on the ground and the Photon Camera that is fixed over the mirror pointing down vertically. The symmetric axes of both components are aligned. The camera is protected against weather conditions with a metallic housing. The metallic holder shown at the *Figure3.8* is used to hold the camera at a specific distance over the mirror.

The bars of the holder cause a shading effect and reduce the total FoV by a small amount. The reduction, which depends on the distance between the vertical bar and the center of the mirror and the distance $d$, is less than $1°$. What is more, the camera itself causes another shading effect. The distance between the lowest point of the camera and the ground is designated as $d$. The loss in the total FoV, called angle $x$, is calculated in case of housing with total thickness 1 cm and in case of no housing. *Figure 3.9* illustrates the scenario. The measured length of the camera is 3.58 cm.

• no housing:

$$\tan(\frac{x}{2}) = \frac{3.58/2}{d} \Rightarrow x = 2\tan^{-1}(\frac{1.79}{d}) \qquad (3.3)$$

• with housing:

$$\tan(\frac{x}{2}) = \frac{4.58/2}{d} \Rightarrow x = 2\tan^{-1}(\frac{2.29}{d}) \qquad (3.4)$$

*Table 3.4* contains the results. There is no difference between the 4 versions of the camera.

| d (cm) | x (º) without housing | x (º) with housing |
|:---:|:---:|:---:|
| 50 | 4.1 | 5.2 |
| 57 | 3.6 | 4.6 |
| 68 | 3.0 | 3.9 |
| 75 | 2.7 | 3.5 |
| 80 | 2.6 | 3.3 |

**Table 3. 4** Loss in the total FoV due to the shading from the camera for different cases.

The smaller the value of *d* is, the bigger the shading is. Of course, the housing increases the shading. So, 154º-156º of the whole hemisphere (180º) can be observed without obstacles.

The mirror is considered as a sphere with radius *r*. The calculated dimensions of System III are *D* and *r* for different values of *d*. *Figure 3.9* indicates these dimensions.

The dimension *D* is calculated using the assumption that the small FoV of the camera should cover ideally the whole mirror.

$$\tan(\frac{smallFoV}{2}) = \frac{D/2}{d} \Rightarrow D = 2d\tan(\frac{smallFoV}{2}) \qquad (3.5)$$
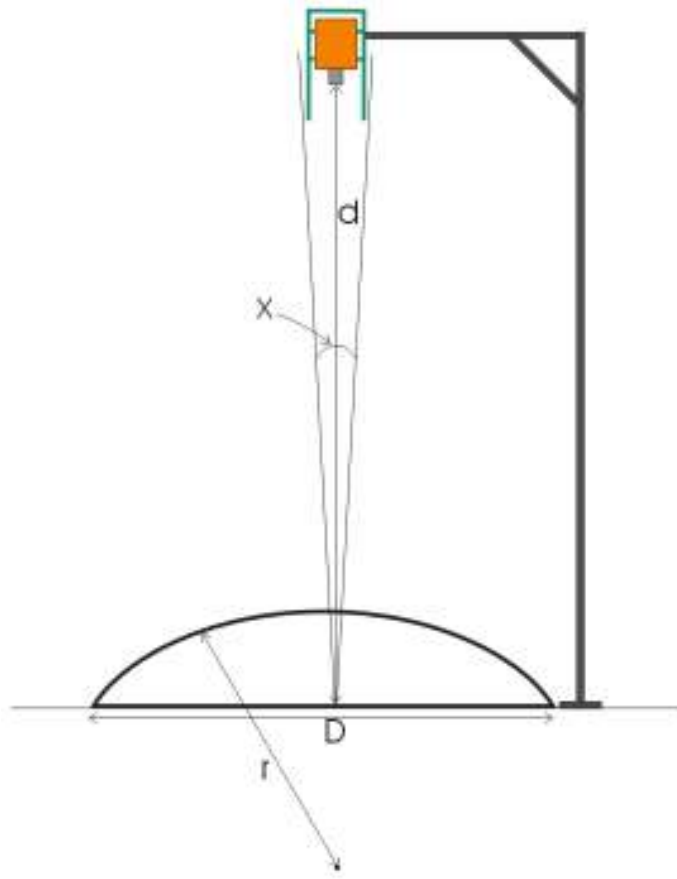
**Figure 3. 9** Calculated dimensions of System III.

*Table 3.5* presents the results as a function of distance *d* for all versions.

| | | D (cm) | | | |
|---|---|---|---|---|---|
| d (cm) | r (cm) | C1 | C2 | C3 | C4 |
| 50 | 11 | 34.4 | 24.0 | 13 | 9.5 |
| 57 | 12.54 | 39.2 | 27.4 | 14.8 | 10.8 |
| 68 | 14.96 | 46.8 | 32.6 | 17.68 | 12.9 |
| 75 | 16.5 | 51.6 | 36.0 | 19.5 | 14.3 |
| 80 | 17.6 | 55.0 | 38.4 | 20.8 | 15.2 |

**Table 3. 5** Radius r of the spherical mirror using C3 and
dimension *D* of the System III for different versions.

The real dimensions are slightly bigger as the FoV covers almost the whole mirror. The size of the mirror increases while the distance *d* increases. Additionally, the bigger the FoV is the bigger mirror is needed. These results come out easily from the laws of geometry. Mirrors with aperture bigger than 25 cm are not suitable mainly because of the high cost.

Further calculations for the radius *r* were made for the version C3 using the small FoV. The method of calculation was based on the following requirement. The beams that are reflected near the edges of the mirror should have elevation $10^o$ from the ground. The *Appendix A* contains the used equations which lead to the final results, as a function of distance *d*, shown in *Table 3.5*

The dimension *r* increases while the distance *d* increases. The diameter of the sphere (2*r) is always bigger than the dimension *D*. So, the used part of the mirror is less than the half of the whole sphere. Regarding the thickness, it is always less than the radius *r* and when d = 80 cm, the worse case, the thickness is estimated about 11 cm.

The system could be implemented using a concave mirror. In this case, the mirror must have a hole in the bottom in order to avoid entrapment of rain droplets. The hole causes extra distortions. So, it is preferable to use a convex one.

## 3. 2. 4  System IV

System IV is another possible implementation of the Cloud Detection System. *Figure 3.10* illustrates the structure of this system. The system contains the Photon Camera which is turned in order to point at the center of the mirror. The convex mirror is placed vertically on a pole. Both components are protected from weather conditions by a metallic housing as shown in *Figure 3.10*. There is a square MIR transparent window (light green line) which allows the electromagnetic waves to enter the construction. This window should be transparent to the infrared radiation. Its material can be one of the proposed for the lens of System I. Note that the one dimension of the MIR transparent window is almost equal to the aperture of the mirror, much bigger than the lens of System I.

System IV has a rotation mechanism with rotating axis the vertical bar. In this way, Photon Camera is able to capture images from the whole hemisphere. Then, the images from a $360^o$ rotation must be stitched together.

**Figure 3. 10** Plot of System IV.

Regarding the total FoV, it is smaller in comparison with the other four systems. This is why the top part of the metallic housing reduces the FoV at least $5^{\circ}$ in one direction. So, the FoV in one direction is about $75^{\circ}$ and due to rotation the estimated maximum total FoV is $150^{\circ}$.

Calculations were held for the aperture of the mirror $D$ for different distances $d$ between the camera and the center of the mirror. The angle of the axis of the camera from the ground is $45^{\circ}$. The dimension $L$ is defined in *Figure 3.10* and is calculated from the following formula:

$$\cos(45^{\circ}) = \frac{L}{d} \Rightarrow L = d\cos(45^{\circ}) \qquad (3.6)$$

The calculations were based on the fact that the small FoV of the camera should cover ideally the whole mirror.

$$\tan(45^{0} - \frac{smallFoV}{2}) = \frac{L - D/2}{L} \Rightarrow \frac{D}{2} = L - L\tan(45^{0} - \frac{smallFoV}{2}) \Rightarrow$$

$$\Rightarrow D = 2L\left[1 - \tan(45^{0} - \frac{smallFoV}{2})\right] \qquad (3.7)$$

*Table 3.6* presents the relevant results.

| version | L (cm) | D (cm) | | | |
|---|---|---|---|---|---|
| | | C1 | C2 | C3 | C4 |
| **d = 40cm** | 28.28 | 29.0 | 21.9 | 13.2 | 9.9 |
| **d = 80cm** | 56.56 | 57.9 | 43.8 | 26.3 | 19.9 |

**Table 3. 6**   Dimension L and aperture *D* of the mirror for different cases.

The real dimensions are slightly bigger as the FoV covers almost the whole mirror. The aperture *D* of the mirror increases with distance *d* and FoV. A practicable mirror can be achieved using C4 and cases of C2 and C3.

## 3. 3   Choice of the catadioptric system

All four proposed systems are more or less suitable for the Cloud Detection System. Each has advantages and disadvantages. The main criterions for the choice are the total FoV, the simplicity of the construction, the protection of the camera against the weather conditions and the cost. Below, there are comments for each system.

*System I:* This system is quite simple in construction and well-protected against rain, snow etc. The total FoV reaches the value of $160^{\circ}$. One possible problem is that the transmittance of the available lenses is not so high and there might be reduction of the power. What is more, because of the small size of the lens, about 2.5 cm, dust and rain droplets cause intense distortions. The total cost of the system seems to be affordable.

*System II: Table 3.3* gives important results for the system. A constructible mirror can be achieved using C4 in distance *d* until 60 cm as the dimension *D* is almost double of the dimension *u*. Note that the real

values of dimension $u$ are bigger that the calculated ones. It is clear that there are few combinations of $u$, $d$, $D$ which fulfill system's requirements. The camera is well-protected against weather conditions. The total FoV is 160$^o$. Finally, a disadvantage of using a concave mirror is that rain droplets might be trapped inside and cause distortions.

*System III:* This system seems to achieve a good proportion of dimensions. A mirror with aperture from 13 to 21 cm and thickness up to 11 cm can be elaborated and has an affordable cost. The maximum total height of the system is about 1 m, an easy to carry construction. Moreover, the camera is protected sufficiently against the weather conditions due to the metallic housing. The whole structure is easily accomplishable. The total FoV is 160$^o$ but 154$^o$-156$^o$ of the whole hemisphere can be observed because of shading effects from the metallic housing.

*System IV:* This system has more difficulties in use. Firstly, the rotation of the system leads to extra mechanical parts, so higher cost and complexity. In order to have a panoramic view of the sky the separate images must be stitched together, which makes the analysis slower. Moreover, a bigger amount of electric power should be consumed due to the rotation. The total cost is unaffordable not only because of the mirror but also because of the big size of the MIR transparent window, which might be 225 cm$^2$. Last but not least, the maximum total FoV is smaller in comparison to the other systems.

All the above mentioned analysis concludes to that the system which is the most appropriate for the Cloud Detection System is System III. In the next paragraphs, there is a detailed review of each component of System III and its final dimensions.

# Description of the Cloud Detection System

## 4. 1  Introduction

This chapter is dedicated to the description of the Cloud Detection System which was chosen in *CHAPTER 3*. Firstly, the dimensions of the system are calculated. It is important to have a sense of the size because it affects the ability to carry it and the total FoV. The system will be used outside and should be easy to place everywhere. Then, there is an extensive analysis of the mirror. The mirror plays a quite important role as such it defines the total FoV and is responsible for distortions. After this study, the most appropriate shape and size are chosen. Finally, there is a presentation of the Photon Camera with important information.

## 4. 2  Geometrical Dimensions of the Cloud Detection System

This paragraph presents the detailed analysis of the configuration used in the Cloud Detection System. *Figure 4.1* and *Figure 4.2* illustrate the structure and the dimensions of each component. The unit of the dimensions is cm. The system contains a metallic box as base consisted of two parts. It was chosen because it was the only available. The mirror is placed on the center of the bigger part. The

hole in the smaller part is due to the construction. The base could be situated on a table. The Photon Camera is mounted inside a metallic housing for its protection against the weather conditions. This kind of mounting is placed in a distance d above the mirror. A holder fixes the camera in this point. The position of the camera is adjustable as such the horizontal part of the holder can be moved using a specific mechanism.
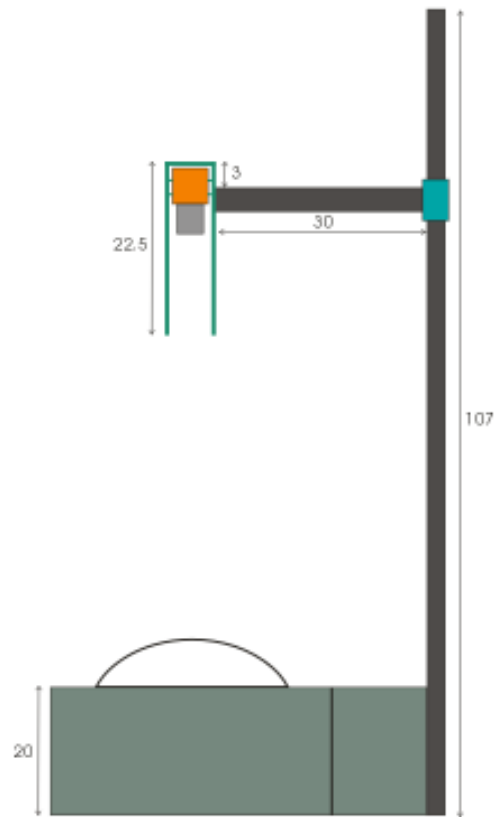


**Figure 4. 1**   Configuration of the Cloud Detection System (dimensions in cm).
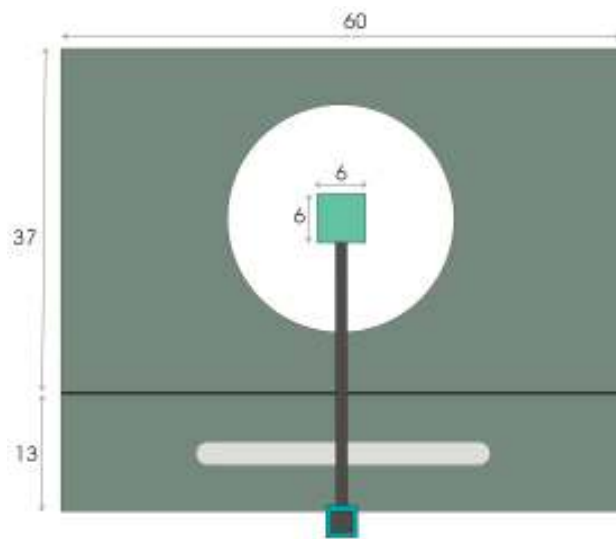


**Figure 4. 2**   Ground plan of the Cloud Detection System (dimensions in cm).

The bars of the holder are compact and have the following dimensions:

|  | width | height | length |
|---|---|---|---|
| **Horizontal** | 1.4 | 2.3 | 30 |
| **Vertical** | 2 | 2 | 107 |

**Table 4. 1** Dimensions of the bars of the holder (in cm).

It is important to make a careful choice of the bars because they cause shading effect. They should be big enough in order to hold constantly the camera but small enough so that they do not cause intent shading effect.

An advantage of the construction is the adjustability of the camera's height. A big variety of shapes and sizes of a mirror could be used by just changing the position of the camera. Regarding the scenario with the spherical mirror analyzed in *paragraph 3.2.3*, *Table 3.6* indicates that placing the mirror in distance d = 57 cm a mirror with aperture D = 14.8 cm is required. In the same way, a mirror with D = 15 cm should be placed in distance d = 57.31 cm from the camera. The last values are a good combination because there is a small impact on the observation from the shading effect, the volume of the system is good enough to carry it and the size of the mirror is financially affordable. Of course, another pair of *D* and *d* could be used and conclude to another shape of the mirror and system configuration.

## 4. 3   The convex mirror

The mirror is manufactured by the company named 'KUGLER GmbH'. Its roughness is < 10 nm. There is no cooling system to avoid its heating. The convex mirror is an important part of the Cloud Detection System. It is used to enlarge the FoV of the Photon Camera from the value of 15$^o$ to the value of 160$^o$. In this way, a hemispherical observation of the sky can be achieved. The quality of the images is depended on various critical parameters such as the coating, the surface quality and the exact shape of the mirror. Images should have sharp edges in order to achieve an accurate detection of the cloud boundaries.  So, a careful study must be done for the definition of mirror's characteristics. In this paragraph,

there is an analytical description of the characteristics of the mirror. Note that the mirror should be cleaned occasionally in order to take away dust etc.

## 4. 3. 1   Shape and size

The shape and the size of the mirror play a significant role in the performance of the system because they determine the total FoV. This paragraph deals with the alternative shapes and sizes of the mirror and at the end there is an explanation for the final choice. Bear in mind that the analysis made in *paragraph 3.2.3* is only to choose the appropriate system configuration and is quite simple. Here, a more detailed analysis is presented. There are two different methods to calculate each parameter. Every method must fulfill a specific requirement. Regarding the size of the mirror, that means its aperture, it is defined by its triangle diameter (see *Figure 4.3*). The use of the triangle diameter ensures that even the further pixels from the center of the camera (at the edges of the orthogonal FoV) will cover a part of the mirror. Triangle diameter is the hypotenuse of a triangle whose the two other sides are calculated in the following way. The big FoV ($20^{o}$) of the Photon Camera should cover the whole mirror. The aperture of this mirror is one side of the triangle. The other side is calculated in the exactly same way but for the small FoV ($15^{o}$). In order to calculate its shape, the small FoV should cover $160^{o}$ of the sky.  So, the nearest to the edges beams, when they are reflected, should have elevation $10^{o}$ from the ground. *Figure 4.4* gives an illustrated explanation of these methods. The blue lines indicate the small FoV, the green the big one and the red the FoV defined by the pixels at the edges of the orthogonal FoV.
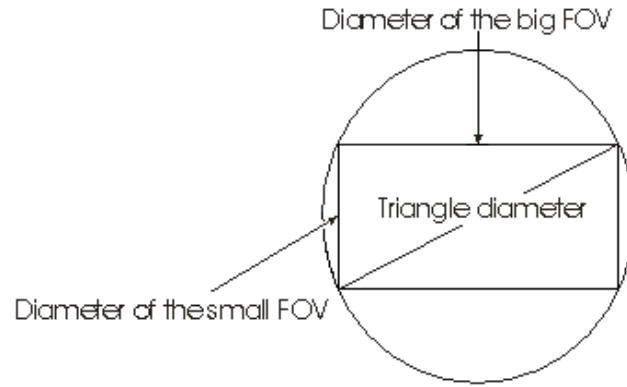
**Figure 4. 3** Calculation of the triangle diameter of the mirror.
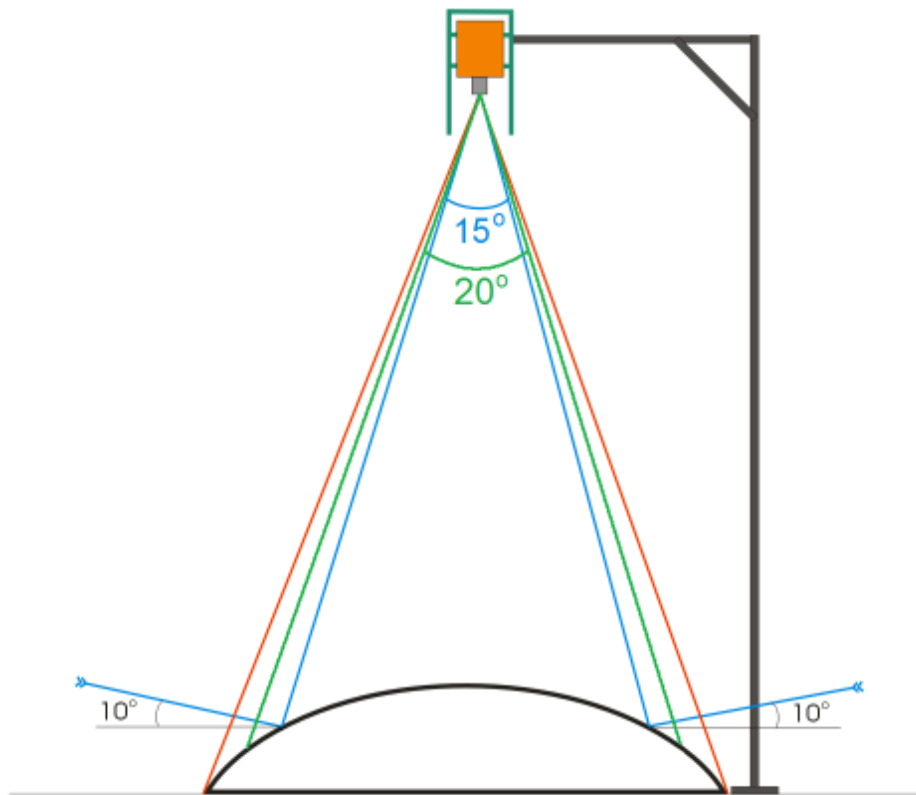


**Figure 4. 4** Illustrated explanation of calculating the shape and the size.

There are several scenarios for the possible shape and size of the mirror. Below, proposals are presented.

Sphere:   The mirror has spherical shape with radius $r$. According to the previous paragraph, the distance $d$ between the mirror and the camera is 57.31 cm. The radius $r$ of the sphere should be 12.6 cm according to *Table 3.7*. The sphere in two dimensions is a circle with radius r = 12.6 cm. The center of the circle is at

the point (0, 0) of a Cartesian coordinate system (x, y). Then, its mathematical formula is:

$$x^2 + y^2 = 158.76$$

(4. 1)

The side of the triangle which corresponds to the big FoV is calculated 20.2 cm while this one corresponds to the small FoV is calculated 15.1 cm. So, the triangle diameter or the aperture is 25.23 cm. The maximum aperture of the sphere is its diameter. But, the aperture is 25.23 cm > 25.2 cm. So, the final aperture of the sphere is 25.2 cm after reducing it 0.3 mm, a negligible amount. It is obvious that the half of the sphere is used and the thickness of the mirror is 12.6 cm. The shape of a sphere is a sufficient choice but not the most appropriate.

Hyperbola:   The shape of hyperbola has various advantages comparing to the sphere. First of all, a more detailed image can be taken. The smaller the covered area of the sky from one pixel is the more detailed the image is. The reason is that the covered area from one pixel is represented on the final image with one single number. According to the theory of Optics and the *paragraph 5.2*, the use of hyperbola leads to higher angular resolution at the periphery and lower at the middle. Higher resolution means that the solid angle of every pixel reduces (see *Figure 5.5*) and information is collected from a smaller part of the sky. This ascertainment is important as the worst spatial resolution is at the periphery (see *Figure 5.7*). That means a bigger coverage of the sky. The angular resolution counterbalances the rapid increase of the spatial resolution at the edges. So, a more detailed image can be achieved at the periphery using a hyperbola in contrast to the spherical mirror.

The calculation method for the formula and the size of the hyperbola is the same with this used for the spherical mirror, keeping the distance d between the mirror and the camera the same. So, the small FoV should cover 160° of the sky. The following mathematical equation in the two-dimension field is used:

$$\frac{y^2}{a^2} - \frac{x^2}{b^2} = 1$$

(4. 2)

The values of parameters $a$ and $b$ are defined by the fulfillment of the requirements. It is important to mention that there are enough combinations of these two parameters that are suitable and not only one. An important parameter of a hyperbola is its eccentricity $e$, which comes out from the following formula:

$$e = \sqrt{1 + \frac{a^2}{b^2}}$$ (4. 3)

It can be considered as a measure of how much the conic section deviates from being circular. *Table 4.2* shows pairs of appropriate values, the corresponding mathematic equation and its eccentricity $e$. All parameters are dimensionless quantities.

| | a | b | equation | e |
|---|---|---|---|---|
| **Case 1** | 46.7 | 21.2 | $0.000458y^2 - 0.0022x^2 = 1$ | 2.41 |
| **Case 2** | 13.1 | 10.43 | $0.0058y^2 - 0.0092x^2 = 1$ | 1.61 |
| **Case 3** | 2.25 | 2.87 | $0.2y^2 - 0.12x^2 = 1$ | 1.27 |
| **Case 4** | 0.52 | 0.71 | $3.7y^2 - 1.98x^2 = 1$ | 1.24 |

Table 4. 2   Parameters and equations of the hyperbolic mirror.

There is another description of a hyperbola from the theory of 'Single-Viewpoint Catadioptric Image Formation'. This description ensures the generation of pure perspective images from the sensed images. [Bak99] It is based on the following equation:

$$\frac{1}{a_h^2}(y - \frac{d}{2})^2 - \frac{1}{b_h^2}x^2 = 1$$ (4. 4)

where, $\qquad a_h = \frac{d}{2}\sqrt{\frac{k_h - 2}{k_h}}$ (4. 5) $\qquad$ and $\qquad b_h = \frac{d}{2}\sqrt{\frac{2}{k_h}}$ (4. 6)

The value $d$ is the distance between the mirror and the camera. So, d = 57.31 cm. The parameter $k_h$ is used for the calculation of $a_h$ and $b_h$ and has no

specific physical meaning. After calculations, the right value of parameter $k_h$ is 7.38. The equation that describes the hyperbola is:

$$y = 28.655 - \sqrt{588.24 + 2.65x^2}$$

(4. 7)

It is important to refer to the description of hyperbolas based on the theory of Conic Sections. This kind of description is widely used, so the *equation 4.4* is converted to its equivalent for the convenience of the reader. Moreover, this form is used by the workshop to manufacture the mirror. According to this description, the shape of a hyperbola is defined by:

$$y = \frac{x^2}{r_h(1 + \sqrt{1 - (x^2 / r_h^2)(SC + 1)})}$$

(4. 8)

where, $SC$ is the Scwarzschild constant and $r_h$ is the paraxial radius of curvature.

The values of $SC$ and $r_h$ which make *equation 4.4* and *equation 4.8* equivalent are the following:

$$SC = -1.38$$
$$r_h = 9.09 \text{ cm}$$

The pair of $SC$ and $r_h$ was calculating by testing various pairs and checking the difference from the arithmetic data of *equation 4.7*. The pair with the less difference was chosen.

Then, the *equation 4.8* takes its final form:

$$y = \frac{x^2}{9.09(1 + \sqrt{1 + 0.005x^2})}$$

(4. 9)

The eccentricity $e$ comes out from the equation:

$$SC = -e^2$$

(4. 40)

and is 1.17. This hyperbola has the same aperture, thickness and eccentricity $e$ as that of the *equation 4.7*.

Regarding the size of the mirror, it is determined by the triangle diameter. As the triangle diameter depends only from the FoV of the Photon Camera and the distance $d$, it has the same value as calculated in the case of sphere. So, the triangle diameter or the aperture of the hyperbola for all cases is 25.23 cm.

The thickness of the hyperbolic mirror changes for every pair of parameters $a$ and $b$ or $k$. *Table 4.3* illustrates the thickness of the mirror for each case of *Table 4.2* and for the *equation 4.7*.

|  | Thickness u of the mirror (cm) |
|---|---|
| **Case 1** | 7.56 |
| **Case 2** | 7.48 |
| **Case 3** | 7.79 |
| **Case 4** | 8.72 |
| **Equation 4.7** | 7.52 |

**Table 4. 3** Thickness of the hyperbolic mirror for various cases.

It is preferable to have the minimum thickness of mirrors which have the same aperture. In this way, the mirror is smaller and has lower cost. Case 2 and *equation 4.7* seem to fulfill this requirement.

For a more thorough comparison, *Figure 4.5* presents the diagrams of hyperbolas for the calculated pairs of parameter $a$ and $b$, for the parameter $k_h$ and of the sphere. The horizontal lines define the bottom part of each mirror. All shapes have common characteristics that derive from the fulfilled requirements. Firstly, all hyperbolas have the same aperture 25.23 cm and sphere has almost the same, which is 25.2 cm. This fact comes out from the common triangle diameter of the mirror. What is more, all shapes have the same tangent at a certain distance from the center. This distance is equal to 7.55 cm and is the consequence of the fact that the small FoV should cover $160^{\circ}$ of the hemisphere. These special points are noticed with two vertical lines on the figure. It is important to notice the difference between the eccentricities $e$. Diagrams of *Figure 4.5* and the values of

eccentricity *e* of *Table 4.2* lead to the following ascertainment: the bigger the value of *e* is the more circular the shape is. Of course, this relationship is accordant to the definition of eccentricity.
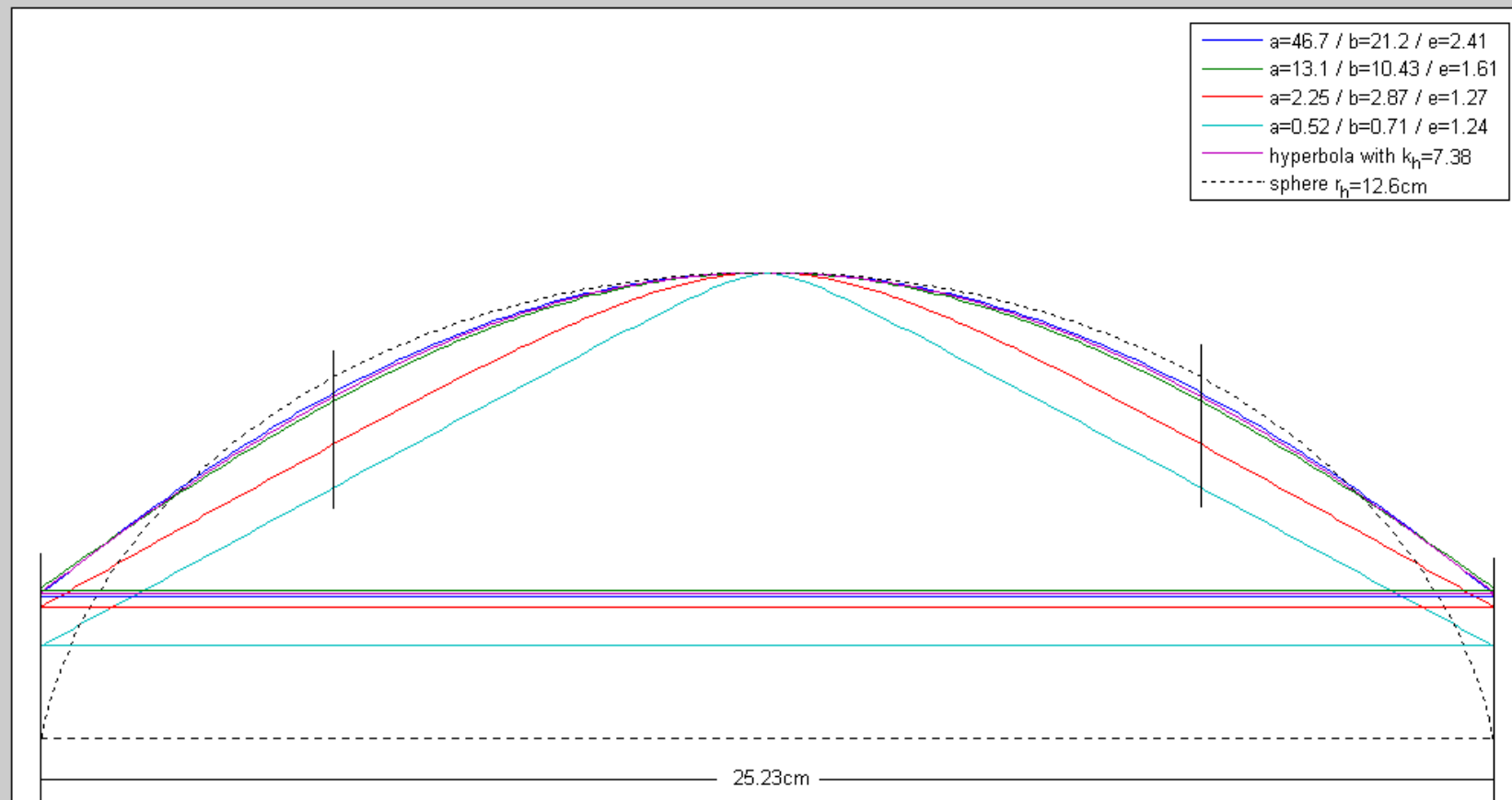
**Figure 4. 5** Possible shapes of the mirror.

Choice of the appropriate shape

A spherical mirror has various drawbacks, as analyzed before, which would be faced with the use of a hyperbolic one. *Equation 4.7* derives from the paper 'Single-Viewpoint Catadioptric Image Formation' which describes the most appropriate hyperbola for capturing purposes. For this reason, this description is chosen for the Cloud Detection System. To be more accurate, the diagram is moved at the y axis so as the mirror is placed at the point (0, 0) of the axis. Then, the final equation of the mirror is:

$$y = 31.78 - \sqrt{588.24 + 2.65x^2}$$

(4. 11)

where, $x \in [-12.615, 12.615]$

*Figure 4.6* illustrates the corresponding shape.
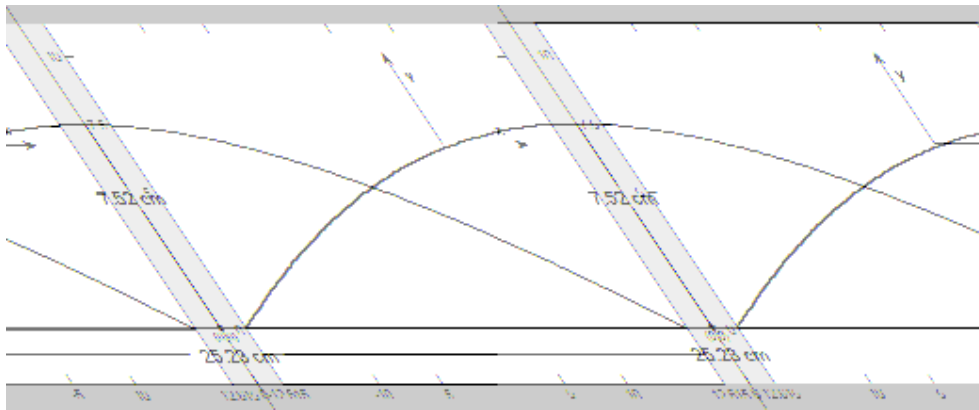


**Figure 4. 6**  The final shape of the hyperbolic mirror.

Notes:

(1)  For a faster and inexpensive fabrication from the workshop, the shape of the mirror can be simulated with a combination of two lines and a circle.

(2)   Due to constructive matters, the real dimensions of the mirror might differ 1-2% from the theoretical values, according to the working experience.

## 4. 3. 2 The constructive material and the coating of the mirror

A basic property of the mirror is its high reflectivity in the MIR region of the electromagnetic spectrum. Low reflectivity leads to absorption of the radiation, low signal-to-noise ratio and heating of the mirror. The body of the mirror is constructed from aluminum 6082. The reason is its essential characteristics, which are described below.

According to its optical characteristics, it is highly reflective in the MIR range. But a more reflective surface is needed. A way to enhance the reflectivity is to use an appropriate coating of the mirror. Several materials have useful optical characteristics and can be used as coatings. Aluminum, gold and silver are the most useful. It is important to mention that the coating is used not only for the improvement of the reflectivity but also it is a protection against weather conditions and increase durability. For instance, these materials have high hardness or are corrosion resistant. All these attributes are described below. Finally, there is a comparison between them and the final choice of mirror's coating.

Aluminum

Aluminum is a widely used material. Below, there are the most important attributes of it:

- highly reflective in infrared wavelengths
- natural coating (oxide)
- almost completely resistant to corrosion
- extremely durable
- not disintegrate when exposed to problematic weather conditions
- strong at low temperatures

*Figure 4.7* is the reflectivity of aluminium in the electromagnetic spectrum. It reflects almost perfect the radiation in the range of 7-10 μm.

Protected aluminium is a special version that resists most damage from normal handling and can be used for coating as well.
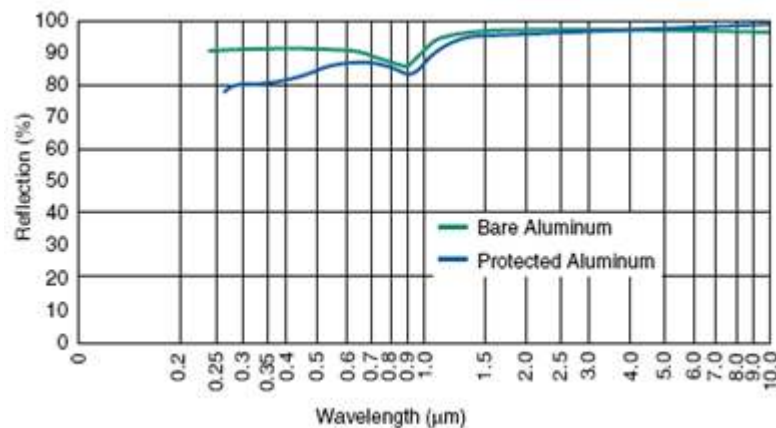


**Figure 4. 7**  Aluminum Reflectance Curve [Eal08].

It is a well-known fact that aluminum does not rust. This is due to the fact that once exposed to air, the surface of aluminum will quickly develop a microscopic thin layer of oxide over its surface, which will make the metal almost completely resistant to corrosion. Thus, the material is suitable for the manufacturing of any object that must remain outdoors for longer periods of time. It will retain its original appearance, along with its structural integrity without much maintenance.

What is more, pure aluminium is soft enough to carve it but mixed with small amounts of other metal to form alloys, it can provide the strength of steel, with only one-third of the weight. It is strong at low temperatures. Although steel becomes brittle at low temperatures, Aluminium increases in tensile strength and retains excellent quality. [Per08]

Silver

Silver has attributes that make it useful for the Cloud Detection System. These are:

- very ductile
- high optical reflectivity
- high degree of polish

Silver is stable in pure air and water, but tarnishes when it is exposed to air or water containing ozone or hydrogen sulfide. Its reflectance curve is illustrated at the *Figure4.8*. It is highly reflective in the range of MIR radiation. [Per08]
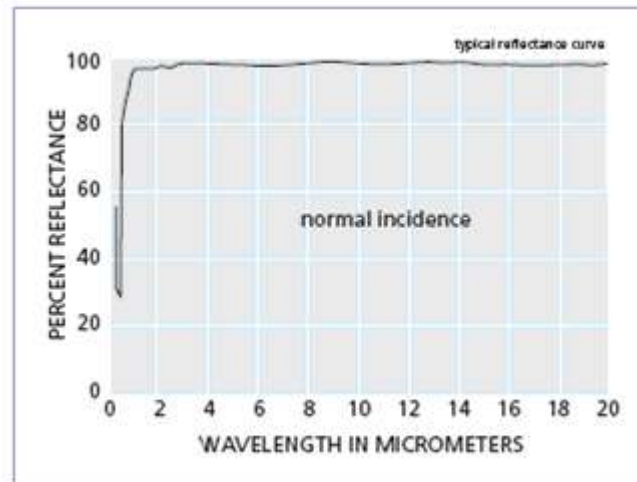


**Figure 4. 8** Silver Reflectance Curve [Mel08].

Gold

Gold is soft, ductile and the most malleable of metals and because of this is usually alloyed to give improved strength and durability. Gold's reflectivity of ultraviolet and visual light rays is low however it has high reflectivity of infrared wavelengths. *Figure 4.9* illustrates its reflectivity. Gold is unaffected by air, nitric, hydrochloric, or sulphuric acid and most other reagents. [Per08]
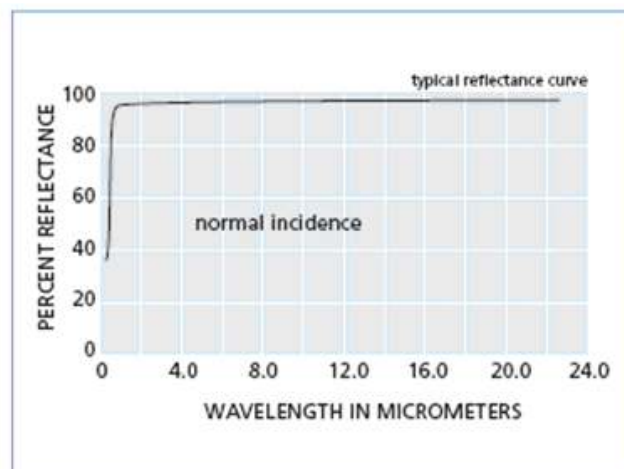


**Figure 4. 9** Gold Reflectance Curve [Mel08].

<u>Choice of the coating</u>

All three alternative coatings fulfill a very important requirement. They are highly reflective in the MIR range. Although, silver tarnishes when is exposed to air or comes in contact with water drops. Tarnishing leads to reduction of the reflectivity and to a blurred MIR image. Moreover, gold and aluminium have quite similar reflectance in MIR region. The company which is responsible for the construction of the mirror proposed a coating made from protected gold as the best choice. It is highly reflective in MIR range and extremely durable.

## 4. 3. 3  Surface quality

Surface quality describes the level of defects that can be visually noted on the surface of an optical component. Surface quality is important because defects can cause light scattering. Surface quality is specified by two numbers, separated by a dash, that relate to the size of the maximum allowed scratch and dig in nm. Experience in optics shows that the surface quality 60-40 is sufficient for most research and scientific applications in the visible and infrared region.

## 4. 3. 4  Surface accuracy

When attempting to specify how closely an optical surface conforms to its intended shape, a measure of surface accuracy is needed. The most common and generally accepted method of judging optics is measuring the error in fractions of light's wavelengths. Companies specialized in optics propose $\lambda/10$ at 10 $\mu$m accuracy for imaging optics requiring low beam distortion. The mirror's surface accuracy for the Cloud Detection System is < 1$\mu$m.

## 4. 3. 5   Weight of the aluminum mirror without the coating

It is important to know the weight $W_h$ of the mirror mainly due to matters of transferring. The mirror could be compact or have a cavity. *Table 4.4* gives arithmetical examples for its weight taking into account only the body and not the coating of the mirror. Bear in mind that the density of aluminum at 20°C is 2.70 g*cm-3.

| Thickness u (cm) | Weight $W_h$ (kg) |
|---|---|
| 0.8 | 1.73 |
| 2.6 | 4.62 |
| 4.8 | 7.11 |
| 6.0 | 7.90 |
| 7.52 (compact) | 9.06 |

**Table 4. 4**   Weight of the mirror for different cases.

The final version of the mirror which is used in Cloud Detection System is the compact one.

# 4. 4   The Photon Camera

The Photon is a long-wavelength (7.5 – 13.5 microns) uncooled microbolometer camera designed for infrared imaging applications that demand absolute minimum size, weight, and power consumption. The manufacturer of the camera is FLIR Systems Inc. It is available in four different versions. Each version has its own FoV and focal length. Even though all four versions are suitable for the Cloud Detection System, the arithmetical results of *Table 3.6* for System III indicate that the most suitable choice is the Photon Camera with FoV 20°x15°. In this way, a system with accomplishable dimensions can be constructed. If a camera with bigger FoV is chosen (C1 or C2), the mirror should be bigger in order to fulfill the requirements. That means higher cost. On the other hand, if the Photon Camera with the smallest FoV is chosen (C4), the used mirror is smaller. That means that the surface of reflection is steeper. The increase of

steepness causes more distortions. *Table 4.5* contains details about the chosen Photon Camera and *Figure 4.10* is a picture of it.

| Focal Length | 35 mm Lens | Length (Lens only) | 9 cm |
|---|---|---|---|
| Field of View | $20^o$ x $15^o$ | Height x Width | 5 cm x 5 cm |
| Performance | <85 mK NEdT | Diameter (maximum) | 42.0 mm |
| Weight | 209 g | Nominal Wavelength | 8.0 – 14.0 μm |

**Table 4. 5**  Technical characteristics of camera C3 [Fli08].



**Figure 4. 10**  Picture of camera C3 [Fli08].

The Photon camera is an export controlled item. In order to increase the Camera's exportability, a 'Slow Video' version of Photon is available. The frame rate is reduced to approximately 9 Hz. This change allows Photon to be exported without US export license to most countries.

## 4. 4. 1   Photon Specifications

• 324 (H) x 256 (V) uncooled, microbolometer sensor array, 38 x 38 micron pixels

• Microbolometer material: Vanadium oxide

• Input power range: 5.0 – 24.0 VDC

• Power Consumption: 1.65 Watts (nominal at room temperature using 8 V input)

• Operating Temperature Range: -40° C to +80° C

• Weight: approximately 97 grams without lens

• Analog video output: NTSC (320x240)/(160x120) or
  PAL (320x256)/(160x120)
  Digital video output: 8- or 14-bit serial LVDS

• Remote camera control RS-232 interface: Photon GUI software (version 1.9.0)

• 2X Digital Zoom with electronic pan/tilt with 324 (H) x 256 (V) sensor array

• Polarity: White Hot

• Dynamic Digital Detail Enhancement (DDE): a filter that causes a sharpening of displayed contrast edges

## 4. 4. 2   Temperature Calibration

Photon includes internal mechanisms for periodically improving image quality via a process called flat field correction (FFC). During FFC, a small calibration flag (a shutter) rotates in front of the detector array, presenting a uniform temperature (a flat field) to every detector element. While imaging the flat field, the camera updates correction coefficients, resulting in a more uniform array output. The video image is frozen during the entire process, which takes less than a second, and it resumes automatically thereafter. Repeating the FFC operation often prevents the imagery from appearing "grainy". This is especially important when the camera temperature is fluctuating, such as immediately after turn-on or when ambient temperature is drifting. Photon provides two FFC modes:

Automatic: In the Automatic FFC mode, the camera performs FFC whenever its temperature changes by a specified amount or at the end of a specified period of time (whichever comes first). When this mode is selected, input windows are available in the Photon GUI for specifying the temperature change and the number of frames that trigger automatic FFC. The temperature change is specified in degrees, with valid values in the range 0 to 100 in 0.1 degree increments. The time period between calibrations is specified in frames, with valid values in the range 0 to 30,000 frames.

Manual: In Manual FFC mode, the camera does not perform FFC automatically based on specified values of temperature change or expired time.

Photon displays, nominally 2 seconds prior to the FFC operation, an on-screen symbol called the Flat Field Imminent Symbol prior to performing an automatic FFC operation.

## 4. 4. 3 Automatic Gain Control

The Photon provides six AGC modes:

Automatic: In Automatic mode, image contrast and brightness are optimized automatically as the scene varies. This mode provides an AGC which is based on a histogram-equalization algorithm.

Once Bright: In this mode, the brightness (level) is calculated as the mean of the current scene at the execution of the command.

Auto-Bright: In this mode, the brightness (level) is calculated as the mean of the current scene just as in 'Once Bright' mode. The difference with 'Auto-Bright' is that the values selected for the start and end of the linear transfer function are automatically updated in real-time, not only at the start of AGC mode selection.

Manual: In this mode, image Contrast (gain) and Brightness (level) are entered completely manually via the sliders.

Linear Histogram: Image contrast and brightness (gain and level) optimized automatically based upon scene statistics using a linear transfer function. The Linear Histogram algorithm uses scene statistics to set a global gain and offset (contrast and brightness) for the image.

Logarithmic: The Logarithmic AGC mode operates identically to the Linear Histogram mode, except that the transfer function applied is Logarithmic as opposed to linear.

### 4. 4. 4   Connection of the camera

The way of connection between the Photon Camera and the PC is illustrated at the *Figure 4.11*.



**Figure 4. 11**   Configuration of the transmission system [Fli08].

The connection is over an Ethernet module. This is an inexpensive and widespread way of connection. Ethernet module gives the ability to place the Cloud Detection System everywhere and transfer through internet the MIR images to the desirable server.

The digital data channel can be configured to output 14-bit data after application of calibration terms. This mode is most useful for external signal-processing and/or analysis of the camera output. The digital channel can also be configured to provide 8-bit data after application of video processing algorithms (e.g. 'Automatic' AGC mode, white-hot/black-hot polarity, image orientation and on-screen symbols). The 8-bit data is essentially a digital version of the video stream provided on the analog video channel and is therefore more appropriate than the 14-bit data for interfacing to a digital display. The digital data channel with output 8-bit data is used during the acquisition of MIR images in *CHAPTER 7*.

The digital data channel employs serial low-voltage differential signaling (LVDS). The channel consists of three signal lines, a clock, a composite sync (frame sync and line sync), and serial data. This is a modern high speed interface employing twisted pair current loop architecture.

Note: the information of *paragraph 4.4* is taken from the manual of the Photon Camera. [Fli08]

# 4. 5   Description of the Cloud Detection System

This paragraph contains various photographs of the real Cloud Detection System. Notes on the images indicate the parts of the system. There is a full description of the system in *Paragraph 4.2*. The mirror shown in the photographs is a dummy one. The final convex mirror is not used in this phase of the development because of a delay from the workshop which is responsible for its construction.



**Figure 4. 12**   Image from the right side.



**Figure 4. 13**   Image from the left side.



**Figure 4. 14**   Image from the front side.
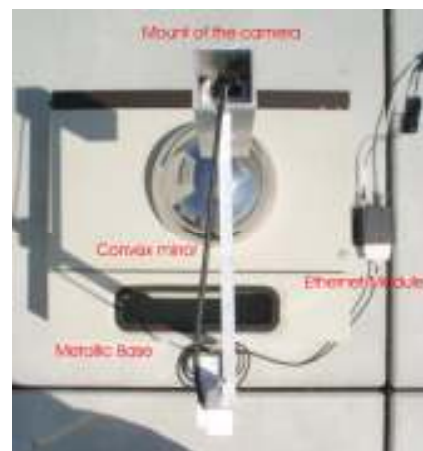


**Figure 4. 15**   Ground plan of the system.

# CHAPTER 5

# System's Performance

## 5. 1   Introduction

The performance of the Cloud Detection System is depended on various critical parameters. There is a need to investigate these parameters and refer to the possible technical problems that might occur. What is more, the ascription of the system can be defined by its resolution and interferences. This chapter deals with the angular and spatial resolution and makes an advisement about the system's interferences.

## 5. 2   Resolution of the Cloud Detection System

There are two kinds of resolution for an optical system: the angular and the spatial. The first one refers to the solid angle of every pixel and the second one to the covered area of the sky by every pixel. Below, there is an analysis of the definition and the values of the two types of resolution.

## 5. 2. 1 Angular resolution of the catadioptric system

In this section, the angular resolution of the catadioptic system is calculated. The angular resolution describes the resolving power of the optical system, which is the ability of the imaging device to measure the angular separation of the points in an object. In simple words, this ability is translated in the change of the solid angle towards the sky of every single pixel of the Photon Camera. Firstly, the angular resolution of the conventional camera, which is the resolution of the Photon Camera itself, is calculated. Then, the angular resolution of the catadioptic system, which is the combination of the Photon Camera and the convex mirror, is estimated. Note that the definitions and the equations are taken from the paper 'A Theory of Single-Viewpoint Catadioptric Image Formation'. [Bak99]

The conventional camera used in the catadioptric system has a frontal image plane located at a distance $u_c$ from the pinhole, the point that each line of light passes through, and that the optical axis of the camera is aligned to the axis of symmetry of the mirror. See *Figure 5.1* for an illustration of this scenario. The axes of the Cartesian coordinate system are (r, z).

Below, there is the definition of the resolution. Consider an infinitesimal area $dA$ on the image plane. If this infinitesimal pixel images an infinitesimal solid angle $dv_c$ of the world, the resolution of the sensor as a function of the point on the image plane at the center of the infinitesimal area $dA$ is:

$$\frac{dA}{dv_c} \qquad (5.1)$$

If $\psi$ is the angle made between the optical axis and the line joining the pinhole to the center of the infinitesimal area $dA$ (see *Figure 5.1*), the solid angle subtended by the infinitesimal area $dA$ at the pinhole is:

$$d\omega = \frac{dA * \cos\psi}{u_c^{\,2} / \cos^2\psi} = \frac{dA * \cos^3\psi}{u_c^{\,2}} \qquad (5.2)$$
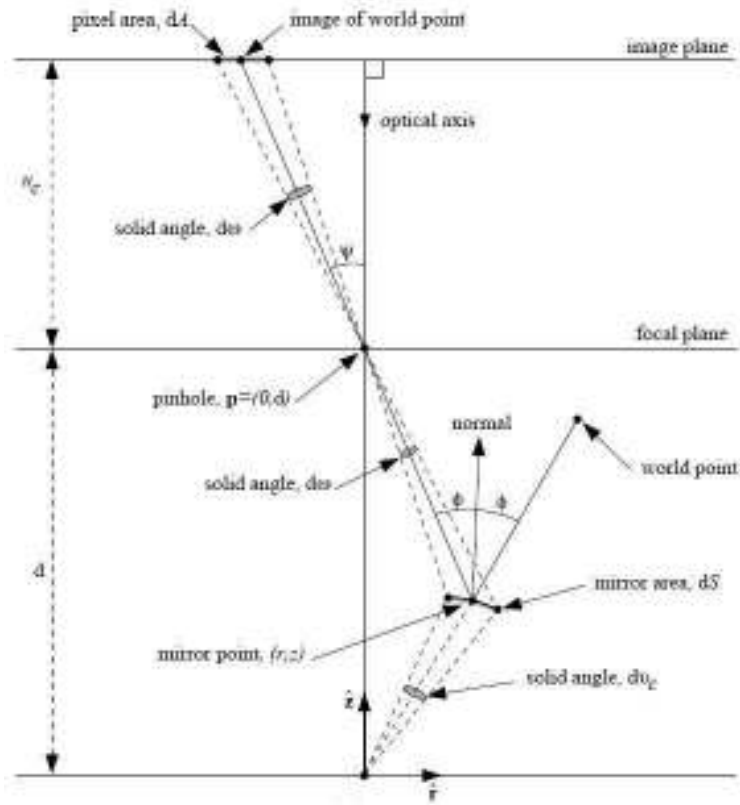
**Figure 5. 1** Geometry used to derive the angular resolution [Bak99].

Therefore, the resolution of the conventional camera is:

$$\frac{dA}{d\omega} = \frac{u_c^2}{\cos^3 \psi} \qquad (5.3)$$

The distance $u_c$ is the focal length of the Photon Camera, so $u_c = 35$ mm. The distance $d$ is the distance between the camera and the mirror and is 57.31cm. The biggest value of angle $\psi$ is 12.4° for the pixels at the edges. The following graph, based on *equation 5.3*, refers to the conventional camera:
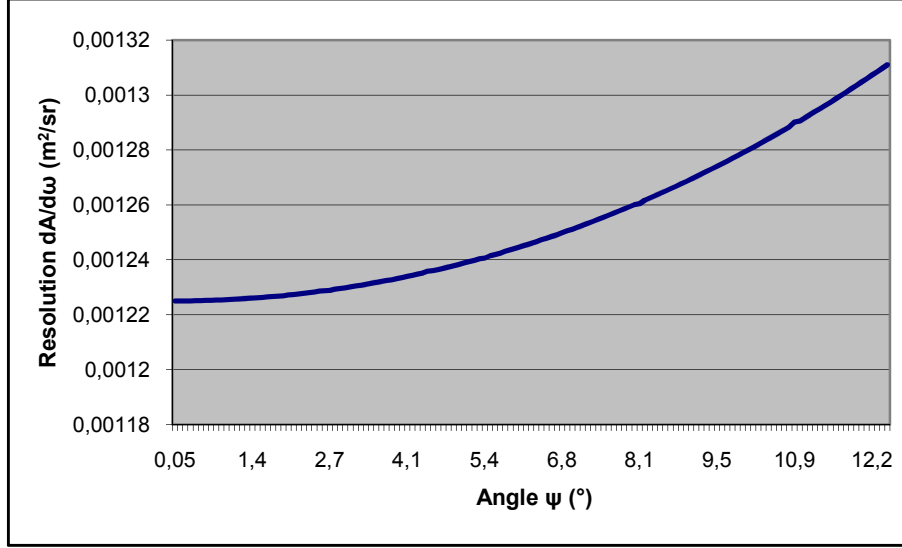
**Figure 5. 2** Angular resolution of the conventional camera.

The pixels are defined from their angle $\psi$. The dimension $dA$ is constant for every pixel. The resolution is bigger when the angle $\psi$ increases. If the camera is pointing to the hemisphere, the pixels at the edges of the image plane will correspond to a smaller angle $\omega$. A small angle $\omega$ indicates bigger resolving power or higher angular resolution. More points in an object can be separated when the boundary pixels are used. The opposite happens near the centre. According to *Figure 5.1*:

$$r_{max} = d * \tan_{max} \psi \qquad (5.\,4)$$

So, $r_{max}$ = 12.6 cm < 12.615 cm. That means the coverage of the mirror surface from all the pixels of the camera. No pixel is unused. The area of the mirror imaged by the infinitesimal area $dA$ is:

$$dS = \frac{d\omega * (d-z)^2}{\cos\phi * \cos^2\psi} = \frac{dA * (d-z)^2 * \cos\psi}{u_c^2 * \cos\phi} \qquad (5.\,5)$$

where $\varphi$ is the angle between the normal to the mirror at (r, z) and the line joining the pinhole to the mirror point (r, z). *Figure 5.3* illustrates the values of $dS$ as a function of the distance $r$ calculated from *equation 5.5*.
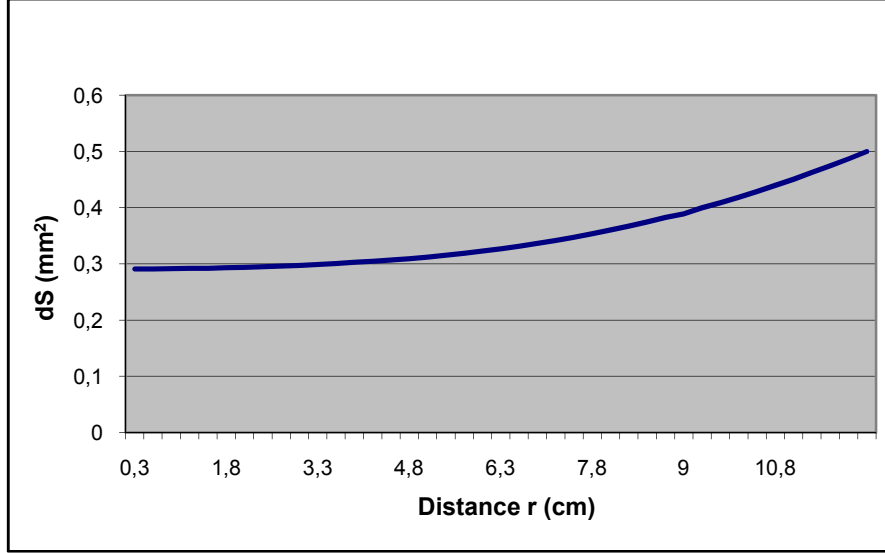
**Figure 5. 3**   Area on the mirror covered by one pixel.

The area of every pixel on the mirror $dS$ increases from the centre to the edges. Since reflection at the mirror is specular, the solid angle of the world imaged by the catadioptric system is:

$$dv_c = \frac{dS * \cos\phi}{r^2 + z^2} = \frac{dA * (d-z)^2 * \cos\psi}{u_c^2 * (r^2 + z^2)} \tag{5.6}$$

Therefore, the resolution of the catadioptric system is:

$$\frac{dA}{dv_c} = \frac{u_c^2 * (r^2 + z^2)}{(d-z)^2 * \cos\psi} = \left[\frac{(r^2 + z^2) * \cos^2\psi}{(d-z)^2}\right] * \frac{dA}{d\omega} \tag{5.7}$$

But, since:

$$\cos^2\psi = \frac{(d-z)^2}{(d-z)^2 + r^2} \tag{5.8}$$

*equation 5.7* takes the following format:

$$\frac{dA}{dv_c} = \left[\frac{r^2 + z^2}{(d-z)^2 + r^2}\right] * \frac{dA}{d\omega} \tag{5.9}$$

Hence, the resolution of the catadioptric system is the resolution of the conventional camera used to construct it multiplied by a factor of:

$$\frac{r^2 + z^2}{(d-z)^2 + r^2}$$
(5. 10)

where (r, z) is the point on the mirror being imaged.

The characteristics of the system illustrated in the following graphs:
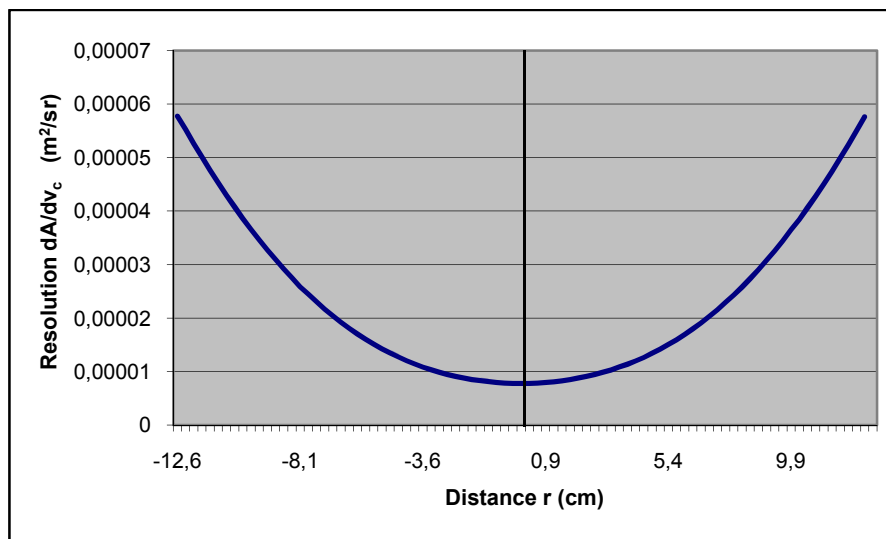
**Figure 5. 4** Angular resolution of the catadioptric system.
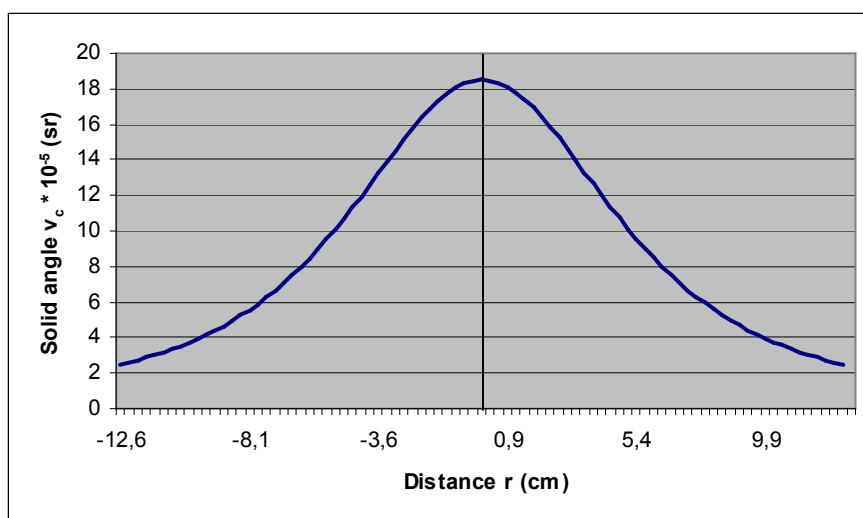
**Figure 5. 5** Solid angle $v_c$ of the catadioptric system.

The pixels are defined by the distance $r$ of the mirror point (r, z) (see *Figure 5.1*). Half of the values of $r$ are negative due to the definition. The dimension $dA$ is constant for every pixel. The angular resolution of the catadioptric system has the same attitude as the resolution of the conventional camera. The resolution increases while distance $r$ increases (see *Figure 5.4*). That means the decrease of the angle $v_c$ (see *Figure 5.5*). Higher angular resolution exists at the boundaries and so more points in an object can be separated. The opposite happens near the centre.

The explanation of the results is the following. In case of a plane mirror, the increase of the distance $r$ from the center leads to the increase of $dS$ and $dv_c$. At a convex mirror, while the distance $r$ increases, $dS$ still increases (see *Figure 5.3*) but $dv_c$ decreases due to the increase of the tangent. The high resolution at the periphery of the hyperbola is beneficial. Refer to the *paragraph 4.3.1* for the advantages of a hyperbolic mirror.

## 5. 2. 2   The spatial resolution of the catadioptric system

In this paragraph, the spatial resolution of the Cloud Detection System is calculated. The spatial resolution is defined as the area $x_s$ of the hemisphere which a single pixel covers. It is a measure of how closely lines can be resolved in an image. *Figure 5.6* illustrates the scenario that is used. The resolution is calculated for $h_c = 2$ km and $h_c = 10$ km. The geometric analysis will be performed in 2-dimensional space. Angle $a_s$, mentioned in *Figure 5.6*, is the elevation of the center of area $dS$ on the mirror from the ground. It is used to define the pixels.
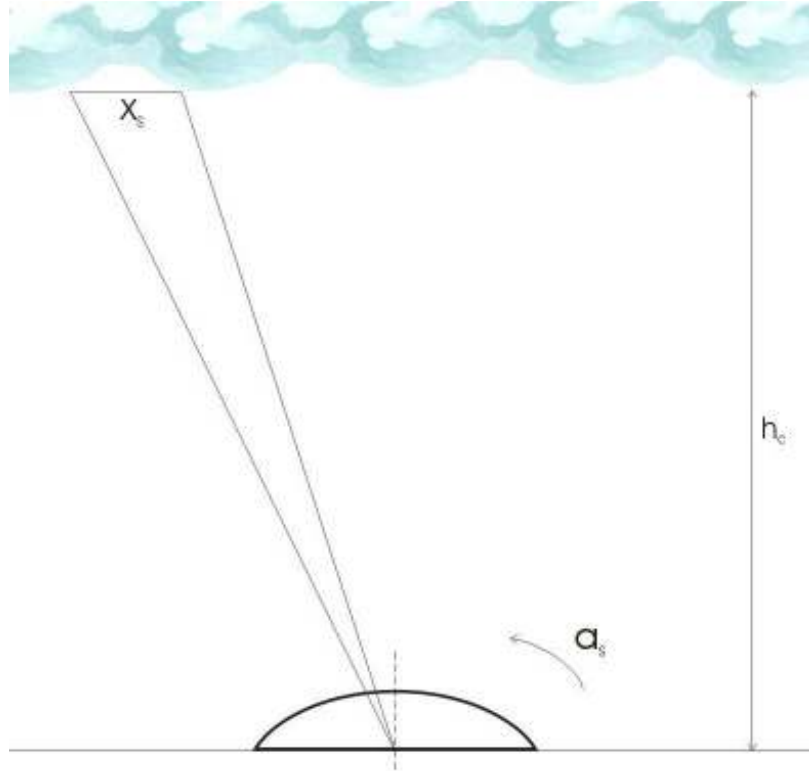
**Figure 5. 6**   Plot used for the calculation of the spatial resolution.

The following graph describes the spatial resolution of the system:
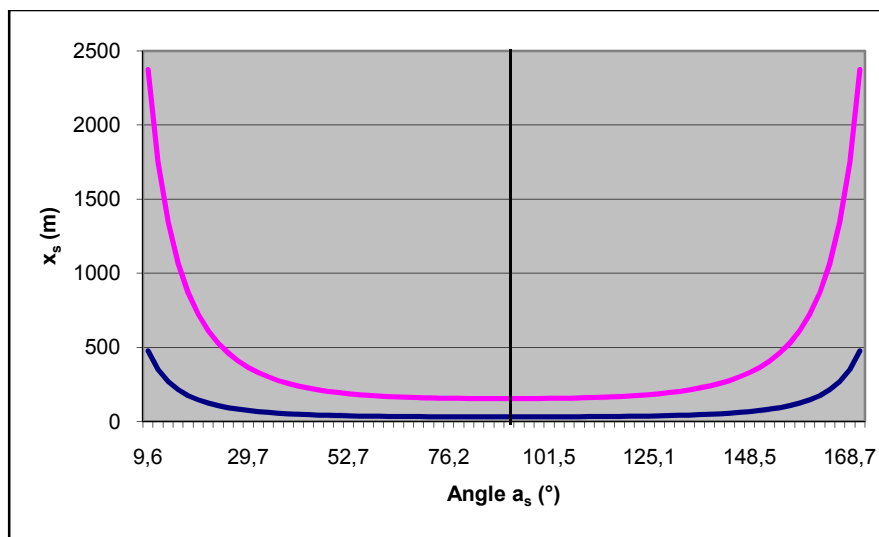


**Figure 5. 7**   Spatial resolution $x_s$ of the Cloud Detection System.

The purple line corresponds to the altitude of 10 km and the blue to the 2 km height. The covered area from every pixel is larger at the altitude of 10 km and, general speaking, when the $h_c$ increases the $x_s$ increases too. This is logic as the bigger radius has a hypothetic circle the bigger chord will correspond to a constant central angle. What is more, the $x_s$ increases at the edges of the image

plane for a specific altitude. The explanation is the same as before as such the pixels at the periphery cover more distant cloudy areas. The opposite happens at the centre of the image plane. The highest resolution is at the center and at low clouds due to the minimization of $x_s$. Higher spatial resolution means that more points in an object can be separated. A hyperbolic mirror has the ability to balance the low resolution at the periphery (see *paragraph 4.3.1*).

## 5.3   Sources of interferences

This paragraph deals with the sources of interferences. There might be interferences from other thermal radiation sources that emit in the bandwidth of 7-14 μm. These sources could be natural or artificial. For instance, the sun emits weakly thermal radiation over the wavelength of 3 μm (see *Figure 5.8*). So, it slightly affects the final image. What is more, the moon is a source of thermal radiation but its spectrum ranges until 2.5 μm. Other natural sources that emit at the range of 7-14 μm, for instance the surface of the earth, could have impact in cloud detection. [Zis96] Moreover, the mirror itself is a source of thermal radiation. The intensity of the radiation is depended on the temperature of the mirror as it emits like a blackbody does. The temperature increases while the mirror absorbs mainly the sun radiation that falls on it. The sun radiates in the spectrum shown in *Figure 5.8*. But, according to *Figure 4.9*, in this range gold is highly reflective, in other words absorbs a very small amount of radiation. So, the mirror coated with gold does not increase its temperature so much and that is why does not emit significant amount of thermal radiation. Other heated metallic constructions in the FoV of the system may cause wrong results. A mask could be applied on the MIR images before their analysis to avoid this incoming noise in the cloud detection. *Paragraph 7.2* deals with this problem.
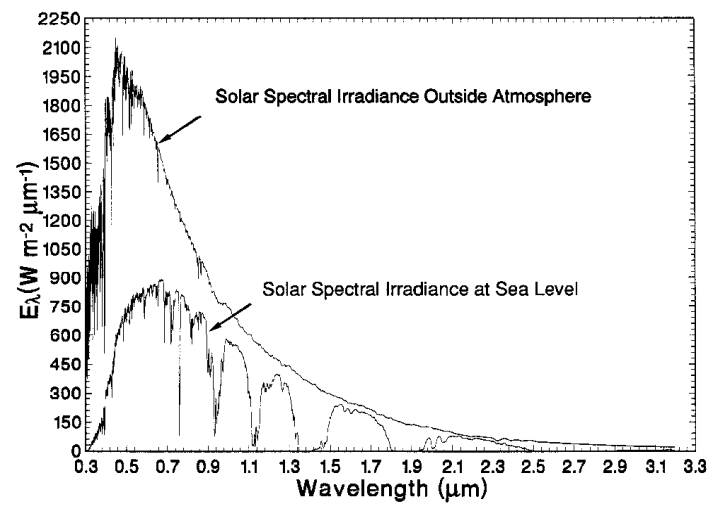
**Figure 5. 8** Spectral irradiance of direct sunlight [Zis96].

# CHAPTER 6

# Software programs

## 6. 1  Introduction

The software used in the Cloud Detection System could be divided into two main parts. The first part is dedicated in the acquisition of the MIR images from the Photon Camera and saving them in a specific directory of the user's PC. The second part deals with the analysis of the saved images, the detection of the clouds and the definition of the cloud coverage. The two programs cooperate so they should have same image parameters, for instance the size of the picture. The cooperation can be implemented in two ways. Firstly, the one program grabs and saves images in a specific directory. Then, the other program searches in this directory and analyzes the saved MIR images. In the second way, 'mex files' of MATLAB can be used. The program which analyzes the images is written in MATLAB. So, it can be started in the command window and, somewhere inside the code, the start of the grabbing program is provoked automatically. The acquired image returns in MATLAB as a matrix. After that, the analysis continuous like the first way. Below, both programs are presented.

## 6. 2 Grabbing and saving MIR images

The company 'FLIR Systems Inc.' provides two graphical user interfaces for the control of the camera. 'Photon GUI' and 'Coyote Application' offer the ability to configure parameters of the Photon Camera, such as the size of the image, the type of grabbing etc, but user does not have the complete control of the system. Main feature of the Cloud Detection System is the real time detection. Both programs first grab all images and then save them, so there is no ability for parallel acquisition and analysis. Moreover, user should adjust the grabbing rate according to his needs. So, a more deep control of the Photon Camera should be applied. The company offers a 'C++ Software Development Kit' (SDK) for building such high-performance applications. It contains modules and classes with which user can build its own code for every specific need. The code is written with MICROSOFT VISUAL C++ 9.0 and is flowchart is the following. *Appendix B* contains the complete code and comments on it. The program can run periodically with time period defined by the user by inserting a count-controlled loop.
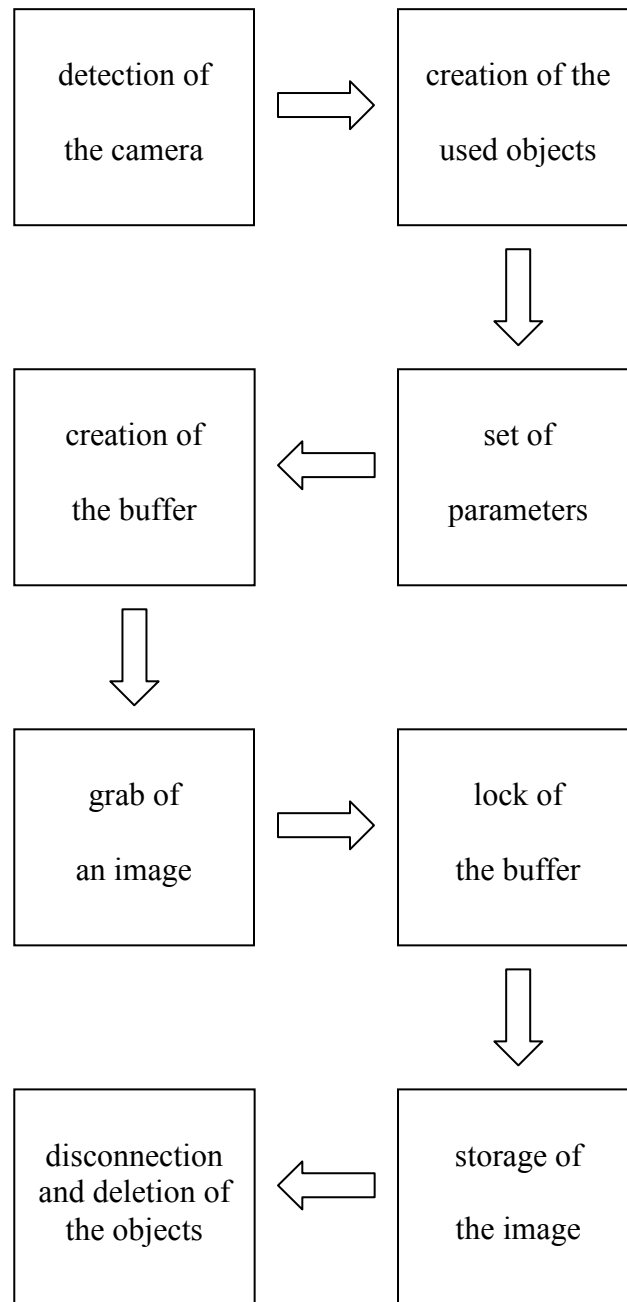
**Figure 6. 1** Flowchart of the grabbing code.

## 6. 3   Analysis of MIR images

The purpose of this code is to detect the clouds in the MIR image, estimate the percentage of the cloud coverage and make a chronological bar showing this coverage. It is written with MATLAB R2008a. The segmentation method is called 'Topological Derivative Segmentation'. Images are segmented using the 'Continuum Topological Derivative algorithm'. The main idea behind this algorithm is to compute the topological derivative for an appropriate functional and a perturbation given by changing the class that a particular pixel is segmented in from one class to another in the set *cls*. This derivative is used as an indicator function to find the best class that each pixel should be classified in. This algorithm is used because it is a fast and efficient way of image analysis. The use of dynamic thresholds gives the ability to achieve a successful analysis for a big variety of cases. What is more, the algorithm can be used for multicolor segmentation (see *paragraph 7.4*). *Appendix B* contains the complete codes of the main function and the 'Continuum Topological Derivative algorithm' and comments on them. The flowchart of the MIR image analysis is presented below.

```
┌─────────────┐          ┌─────────────┐
│  load of the│          │  load and   │
│             │  ═══>    │application of│
│  MIR image  │          │the gain filter│
└─────────────┘          └─────────────┘
                                │
                                ▼
┌─────────────┐          ┌─────────────┐
│ segmentation│          │  load and   │
│ of the MIR  │  <═══    │application of│
│   image     │          │  the mask   │
└─────────────┘          └─────────────┘
      │
      ▼
┌─────────────┐          ┌─────────────┐
│calculation of│         │  storage of the│
│  the cloud  │  ═══>    │ analyzed MIR │
│  coverage   │          │ image and data│
└─────────────┘          └─────────────┘
                                │
                                ▼
                         ┌─────────────┐
                         │creation of the│
                         │ chronological│
                         │    plot      │
                         └─────────────┘
```
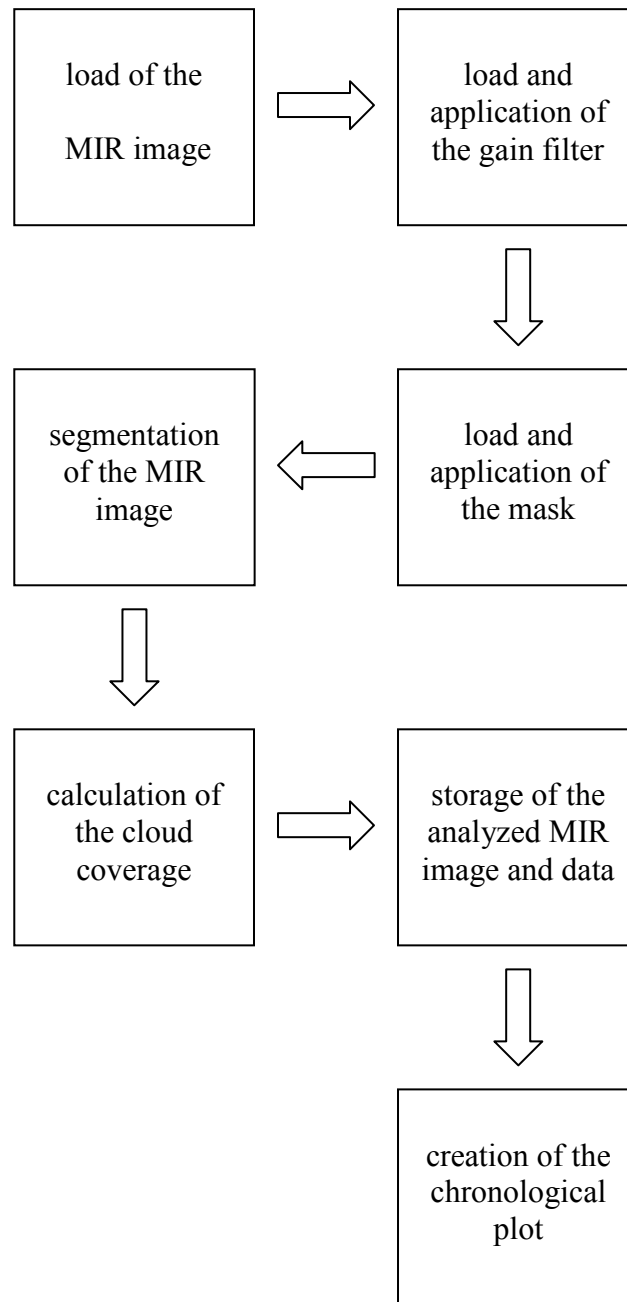
**Figure 6. 2**   Flowchart of the MIR image analysis.

# CHAPTER 7

# MIR image analysis

## 7. 1  Introduction

The analysis of MIR images is the most important part of the Cloud Detection System. Information about the performance of the system and the cloud coverage of the sky can be exported. Cloud detection faces various problems coming mainly from the environment and the conditions at the sky. Masks and filters can be applied on the MIR images before their analysis in order to avoid problems in the segmentation. What is more, sun is displayed as a bright object on the images. So, its impact should be studied. *CHAPTER 7* deals with the mentioned topics. It contains also various examples of analyzed images, image segmentation using 2 and 3 colors and extreme problematic cases. Finally, a real scenario is presented. According to that, images are grabbed every hour and a chronological diagram, which describes the changes of the cloud coverage during the day, is created. Cloud statistics and cloud amount can provide important information to climate models to help understand the role of clouds in atmospheric radiation. The whole analysis is made using the method of *CHAPTER 6*. A point to be noted in the results is that the statistics can change if the parameters of the codes change. The parameters used ensure the best results. MIR images were taken at Oberpfaffenhofen in Germany during the period of June 2008.

Note: due to a delay in deliverance of the mirror, the dummy mirror, which is shown in *Figure 4.12*, is used for taking MIR images. Results will be more accurate using the appropriate one.

## 7. 2   The mask

Surrounding of the system may contain objects with high temperature which emit more infrared radiation than clouds. Usually this happens with metallic constructions during sunny days and the surface of the earth. This situation leads to wrong cloud detection as the program considers the bright object as a cloud. Moreover, because of the high intense of infrared radiation from the structure, 'Continuum Topological Derivative algorithm' classifies clouds at the black part of the final image instead of the white one. For correct cloud detection, a mask on the acquired images should be put before their analysis.

The following images are various scenarios illustrating the problem. *Figure 7.1* is an image taken from the Photon Camera. Surroundings cover a big part of the image and are displayed bright. The vertical bar of the holder is displayed too. Clouds exist at the sky but the implementation of the segmentation algorithm leads to *Figure7.2*. The results are completely wrong. Cloud area is black indicating a completely clear sky while buildings and a small part of the vertical bar are displayed with white color and detected as clouds. Same results can be excluded for the second scenario. *Figure 7.3* displays a big metallic construction and a part of the earth surface. Both emit high infrared radiation in comparison to clouds that are darker. The analysis without filter leads to *Figure 7.4*. It is obvious that the results do not correspond to the real situation.

The next step is to apply a mask on the *Figure 7.1*. The mask can be created by painting black bright objects and the rest part white. The conjunction of the mask and the MIR image is made automatically by the function 'cloud_coverage_statistics' (see *paragraph 6.3*). *Figure 7.5* illustrates the masked image and *Figure 7.6* the analyzed masked image. The problem with bright objects is solved. Heated constructions are displayed with black colour and only clouds are in the white area. Here, there is another critical point in the analysis. Even though, there are clouds in the central part of the MIR image, the algorithm can not distinguish them. Special filters are needed to improve the image analysis. Next paragraph deals with this kind of procedure. A mask covering the earth surface and the metallic tower could be also used in the second scenario in order to take the right results. A new mask should be created every time the place of

measurement changes. The basement should be stable and constant because a small change in the place of the system means new mask. Moving bright objects can not be manipulated. Hopefully, they cause temporary errors.



**Figure 7. 1** MIR image of the hemisphere before applying the mask (scenario 1).
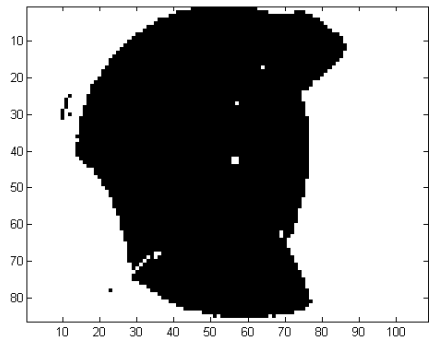


**Figure 7. 2** Analyzed image of scenario 1 before applying the mask.



**Figure 7. 3** MIR image before applying the mask (scenario 2).
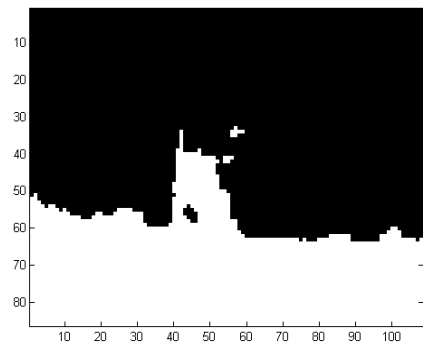


**Figure 7. 4** Analyzed image of scenario 2 before applying the mask.
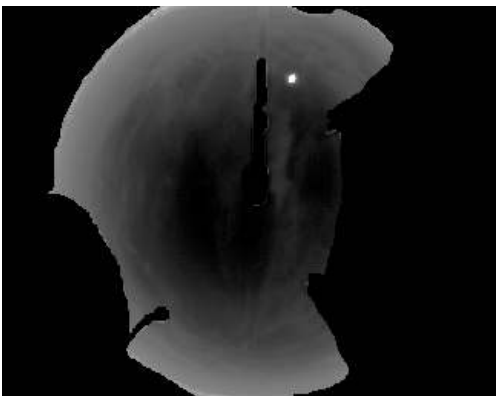


**Figure 7. 5** MIR image of the hemisphere after applying the mask (scenario 1).
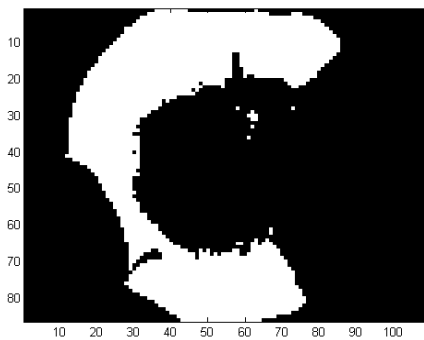


**Figure 7. 6** Analyzed image of scenario 2 after applying the mask.

## 7. 3   The gain filter

*Paragraph 5.2.1* describes the angular resolution of the catadioptric system. The solid angle $v_c$ is bigger in the middle of the mirror and decreases at the edges (see *Figure 5.5*). Central pixels collect more power in comparison to the boundary ones as they correspond to bigger solid angles. A gain filter is applied on the masked MIR image in order to achieve a more equable distribution of the power. This filter reduces the power in the center and increases it at the edges. So, its boundaries should be brighter than its middle. The shape is radial in order to be coherent with the radial uniformity of the solid angle $v_c$. The gain filter is applied automatically by the function 'cloud_coverage_statistics' (see *paragraph 6.3*). Two different filters are examined. Figures below illustrate these two alternatives. Analyzed images show that using filter 1 more clouds are detected. The percentage of cloud coverage is 28.68 % for filter 1 and 27.64 % for filter 2. So, filter 1 is used for correction of the power distribution. *Figure 7.9* shows how should be the MIR image before running the 'Continuum Topological Derivative algorithm'.

**Figure 7. 7**  Gain filter 1.
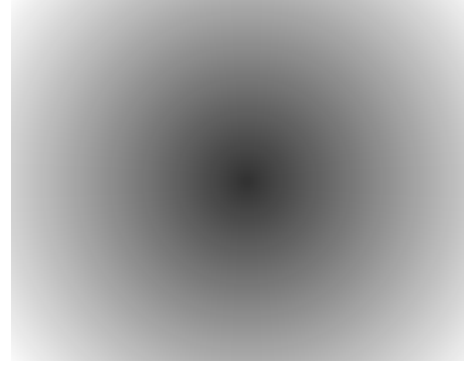


**Figure 7. 8**  Gain filter 2.
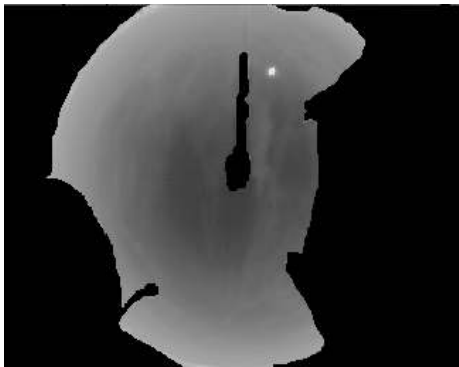


**Figure 7. 9**  Masked MIR image with filter 1.
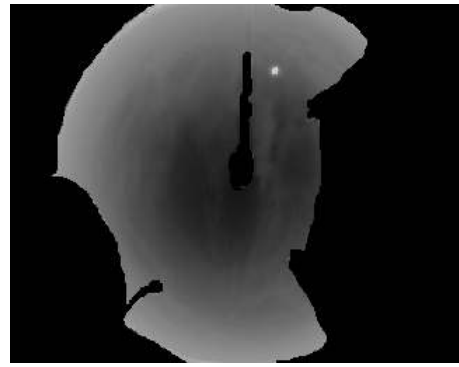


**Figure 7. 10**  Masked MIR image with filter 2.
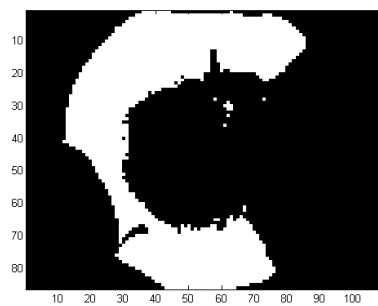


**Figure 7. 11**  Analyzed masked MIR image
with filter 1.
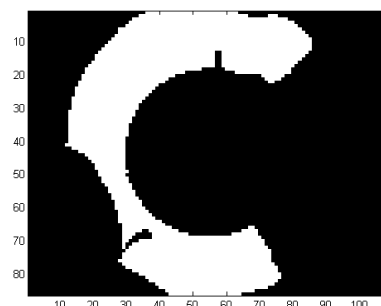


**Figure 7. 12**  Analyzed masked MIR image
with filter 2.

## 7. 4  MIR image analysis using 3 colors

Sometimes there is a need not only to detect clouds and define the cloud coverage but also to distinguish clouds according to their thickness. In this paragraph, a measurement, which classifies clouds into two categories using 3 colors, is presented. The analysis could be extended using more colors, which means more categories of cloud thickness and more accurate observation.

The number of colors can be set by changing the parameter *cls* of the function 'Segmentation_Continuum_TD'. By setting cls = 3 the final image has 3 colours; black for no clouds, grey for thin clouds and white for thick clouds. The reason is simple. Thin clouds have less mass. So, they emit less radiation than thicker clouds in the same temperature. They can be classified neither in the white part as they do not have so much intensity nor in the black part in which belongs clear sky. So, they are classified in the middle category and symbolised with grey colour. Below, there is an analysis of an MIR image using 2 and 3 colours.



**Figure 7. 13**  MIR image of the sky.
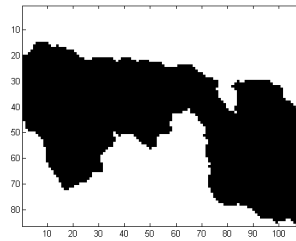


**Figure 7. 14**  Analyzed MIR image using 2 colors.
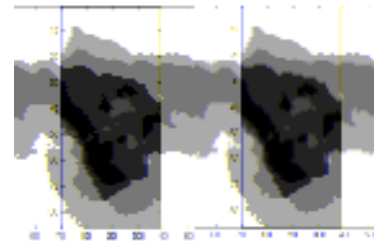


**Figure 7. 15**  Analyzed MIR image using 3 colors.

The feeble parts of the original image correspond to the grey parts of the final figure. More colours illustrate the variation in thickness as in *Figure 7.14* thin and thick clouds are considered the same. This information is important because thick clouds mainly damage the signal. So, the problematic areas of the sky could be separated. Using 3 colours cause a more accurate cloud detection as thin clouds of *Figure 7.13* correspond to black area of *Figure 7.14* but to grey area of *Figure 7.15*. This method is useful for the understanding of the physical characteristics of clouds. It is advisable to be avoided when the purpose is the cloud coverage of the sky. The loss in cloud detection using 2 colours is negligible as the undetected clouds are the thin ones that are not so harmful for

the signal. Note that the terms 'thin' and 'thick' clouds have nothing to do with the meteorological terminology.

## 7. 5   Chronological analysis of cloud coverage

One main implementation of the Cloud Detection System is the collection of statistics of the cloud coverage. In this way, the climatic conditions of an area for a large period of time can be defined, during the day and night, due to the infrared camera. Moreover, the suitability of an area for establishment of a telecommunication system can be evaluated or an instant estimation for the performance of a wireless link can be made. Cloudy atmosphere leads to signal distortions and attenuation. Perhaps, an automatic change of the ground station to another under clear sky improves the data transfer.

Here, a real scenario is presented. MIR images are acquired every one hour from 10:00 to 16:00. The camera is pointed direct to the sky without the usage of the mirror. There is no need to use a mask and a gain filter. Similar analysis can be performed using the convex mirror, a mask and a filter. *Figure 7.16* shows the hourly-acquired MIR images and their analysis.



| 10:00 | 11:00 | 12:00 | 13:00 |



| 10:00 | 11:00 | 12:00 | 13:00 |
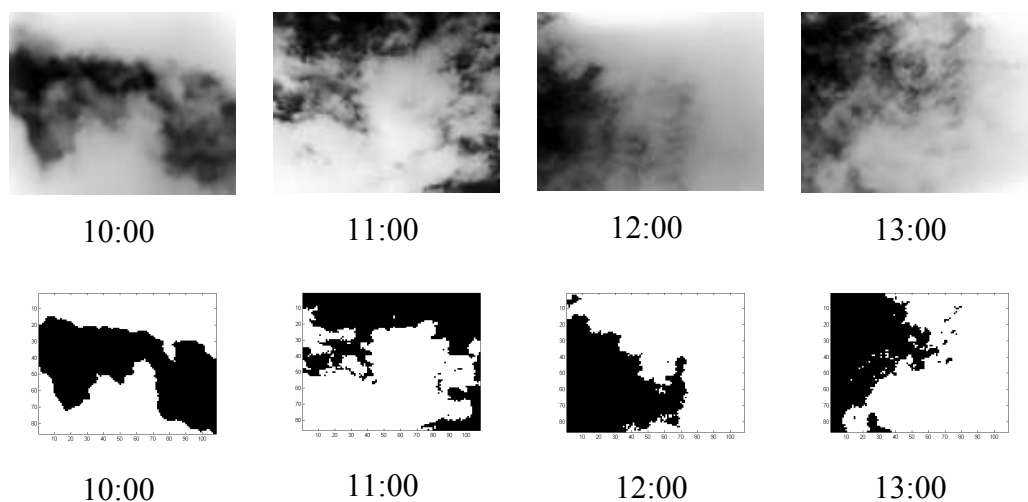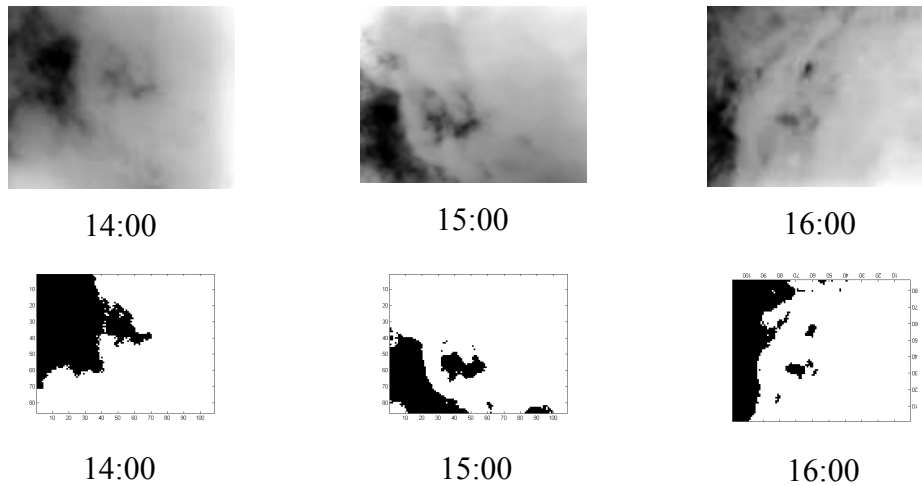
**Figure 7. 16**   Hourly-acquired MIR images and their analysis.

The software programs developed in *CHAPTER 6* calculate the percentage of the sky which is covered by clouds and save data into the 'Coverage.txt' file. Then, MATLAB program creates a chronological plot using these data. The plot of the scenario is presented in *Figure 7.17*.
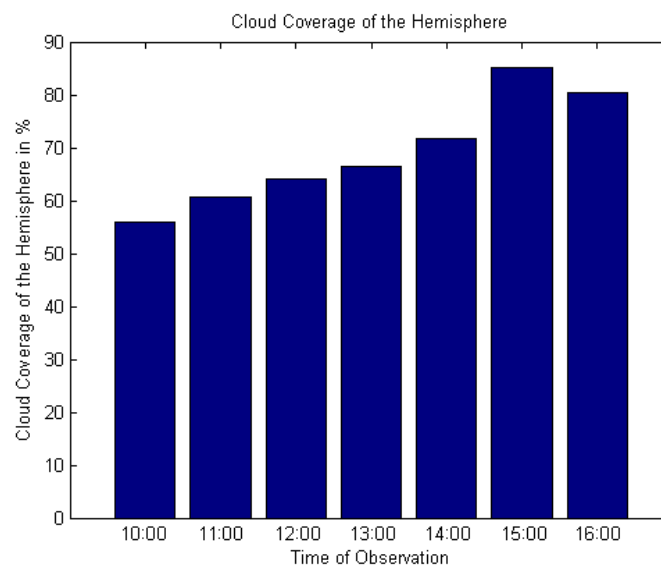


**Figure 7. 17**   Chronological change of cloud coverage per hour.

The method could be implemented for bigger time periods or statistics per week, month etc. can be extracted after further process.

# 7. 6  Clear and overcast sky – System Calibration

There are various cases in which cloud detection faces obstacles. The segmentation does not correspond to the real case. That happens in cases of clear or overcast sky. Figures below illustrate well the errors.



**Figure 7. 18**   MIR image of clear sky.
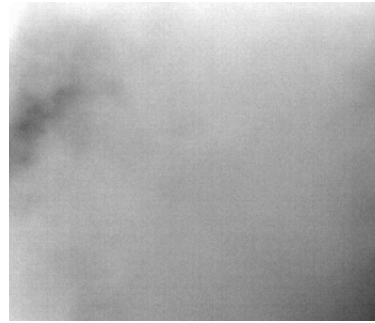


**Figure 7. 19**   MIR image of overcast sky.
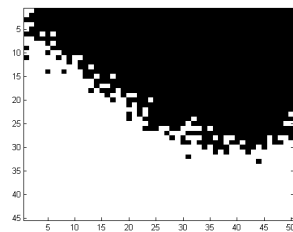


**Figure 7. 20**   Analyzed image of clear sky.
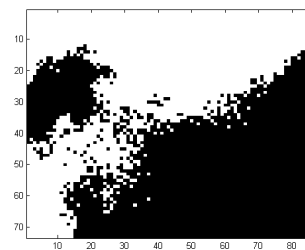


**Figure 7. 21**   Analyzed image of overcast sky.

*Figure 7.20* shows a sky half covered with clouds. This estimation is completely wrong as the sky of *Figure 7.18* is clear. What is more, only half clouds of *Figure 7.19* are detected in *Figure 7.21*. Program is weak to manipulate these cases. The weakness derives from way the functions work. Every class has an optimised value which depends on the range of pixels' intensity.  The less uniform the MIR image is the wider the range is. Wide range of values leads to big differences between the optimised values of the classes. Software checks the intensity of every pixel and puts it in the class from which differs less. Pixels with similar intensity, for instance pixels of a cloud, have higher probability to be included in the same class when the optimised values are well distinguished. Classes in case of clear or overcast sky are near because the small range of pixels' intensity. All pixels have almost the same intensity but it is quite possible to be

symbolised with different colours due to the small distance between the optimized values. In this way, pixels of overcast sky are detected as clear sky and reversely.

System needs correction methods to overcome this problem. Here, the most important are presented.

- User could have a backup of images from clear and overcast sky. Clear sky and cloud temperature varies not only during the day and night but also from season to season. Pictures from various time periods of the year and time points of the day should be acquired in order to cover most of the cases. Before the segmentation of the MIR image, the software program could compare the grabbed image with the images from the backup. This could be done by comparing each pixel one by one of both images. If the program finds similarities, a message could be displayed informing for a clear or overcast sky and 0% or 100% cloud coverage correspondingly. It is essential to achieve a fast way of comparisons.

- A similar method to the previous one is the usage of blackbody models. Clear or overcast sky has almost a constant temperature. Then, it could be considered as a blackbody with the same temperature. *Paragraph 2.4* contains the theory on which this assumption is based. Plots of emission for various temperatures could be created using Plank's law (see *equation 2.1*). Afterwards, the same method of comparison as before could be followed.

- Images of a clear or overcast sky are uniform and their pixels have similar values of intensity, which is an important characteristic. Before the analysis of the MIR image, an algorithm which gives statistic parameters of the intensity could be applied. For instance, if the fluctuation of the pixel intensity is small, pixels of the image have a narrow range of intensity. This is serious evidence in order to conclude that the MIR image comes from a clear or overcast sky.

- Using statistics from different cases of clear or overcast sky, the mean temperature for each condition can be defined. These two values, the mean temperature of clear and overcast sky, could be used for the calibration of the system. Two emission models of blackbodies are created, one using the mean temperature of clear sky and one considering this of overcast sky. *Paragraph 2.5* is a good example of creating such models. The following procedure takes place before every image segmentation. First, the corresponding amount of radiation from a blackbody which has the mean temperature of clear sky is abstracted from the intensity of every pixel of the MIR image (see *Figure 2.16*). If the result is near zero, the original image comes from clear sky. If not, the abstraction is repeated but now taking into account a blackbody with the mean temperature of overcast sky. The original image shows an overcast sky in case of nilpotent rest. In any other result, clear and overcast sky cases are excluded and MIR images are segmented as described in *CHAPTER 6*.

## 7. 7   The impact of the sun on image segmentation

Sun emits infrared radiation as well. During the day, sun is always in the field of view of the Cloud Detection System. So, there is a need to study how it affects the final results. The following figures describe a sequence of MIR images taken for this purpose.
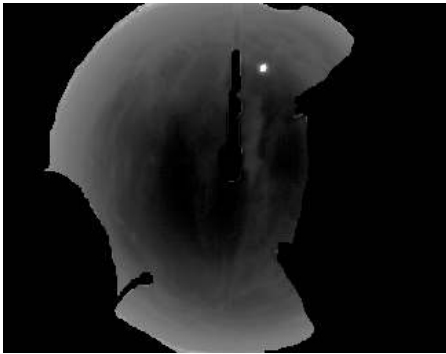


**Figure 7. 22**   Masked MIR image with sun.
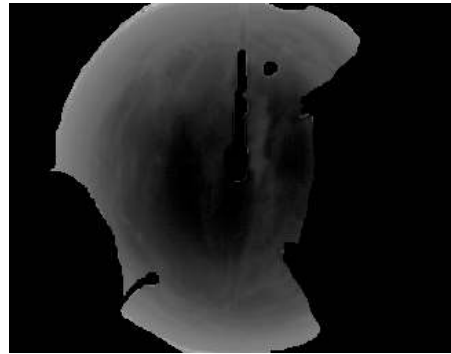


**Figure 7. 23**   Masked MIR image without sun.
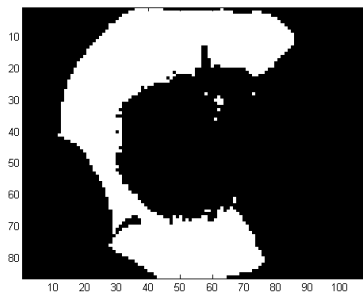


**Figure 7. 24**   Analyzed image with sun.
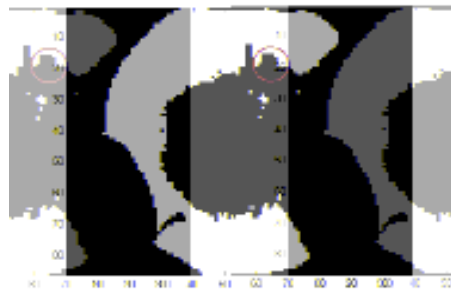


**Figure 7. 25**   Analyzed image without sun.

The results show that in case of the presence of the sun, cloud coverage is 28.68 % and in case of its absence is 28.48%. The only impact of the sun radiation is the increase of the cloud coverage by the sun area (red circle of *Figure 7.25*). This change is negligible and always constant during the day. So, it is easy to manipulate it. Note that sun does not affect the formation of the classes in the segmentation functions.

<div align="right">

# CHAPTER 8

# Conclusion

</div>

## 8. 1   General Results

In this thesis, a Cloud Detection System with hemispherical observation is developed and tested. Firstly, all the possible structures of the system are analyzed and the most appropriate is chosen. A study was held for the components of the system and the software programs. The system is used in various sky conditions. Cloud statistics and cloud amount have been calculated with the available date. Theses statistics can contribute to the understanding of climate models.

The dimensions and the weight of the system are good enough in order to be carried and placed in various locations. The vertical bar of the holder is adjustable and in this way the same structure can be used for various types of mirrors if it is moved properly. The desired results are achieved without increasing the complexity of the structure. Moreover, the camera is well protected against weather conditions, important matter especially during winter. The mirror is highly reflective in infrared radiation and produces total FoV of $160^{\circ}$ covering the important part of the hemisphere. Ethernet module gives the ability to plug in the camera everywhere in any distance and control it always from the same place.

The results show a successful development of the system and an effective performance. System using masks and filters, in order to correct the uninformed angular resolution, detects accurately mainly thick clouds, which have the biggest impact in the signal. Thin clouds could be also detected using more than two colors in the analyzed image. User can have a good overview of cloud coverage changes using chronological plots (see *Figure 7.17*). The analysis can be

performed parallel to image acquisition. So, an instant evaluation of sky conditions can be made.

A special characteristic of the system, that alters it from previous efforts, is the Photon Camera which works in the range of infrared radiation. In this way, the system is functional 24 hours per day. So, during the night, optical links can be evaluated and statistics can be collected. The cost of the mirror, the camera and the software is about 11,500 €.

## 8. 2  Further Research

Various problems, regarding the cloud detection, occurred during the measurements. As mentioned in *Paragraph 7.6*, clear and overcast sky can cause wrong detection. There are proposed various methods of improvement. A further research should be made in this direction. These methods decelerate the image analysis. So, a faster algorithm for image analysis should be developed.

Another point that needs improvement is the manipulation of bad weather conditions. For instance, drops of water on the surface of the mirror may cause distortions. A possible solution is to place a heating system under the mirror in order to evaporate drops. Moreover, a mechanism for the rotation of the mirror could be implemented. In this way, images from the sky for different positions of the mirror could be taken and, then, stitched together in order to get rid of the droplets or dust. The study of such mechanism should be careful as the complexity of the system increases.

MIR images were taken using a dummy mirror due to a delay from the workshop. Measurements should be repeated using the mirror illustrated in *Paragraph 4.3*. The results will be more accurate than those presented in this thesis.

Image capture and cloud detection are not completely implemented. Further work should be made for their completeness. For instance, this version of the system can detect cloud with frequency 1 minute. The final aim is the cloud

detection per 10 seconds. Regarding the mask, it could de created automatically by applying the segmentation algorithm on the original MIR image. The image is segmented in two parts, the heating objects defined with white and the sky defined with black. Then, the colors are reversed and the processed image is combined with the original one. The segmentation algorithm is repeated in order to detect the cloud this time.

# Appendix A

## A. 1 Calculations for *Table 3.5*

The following figure is useful for the calculation of parameter *r*.
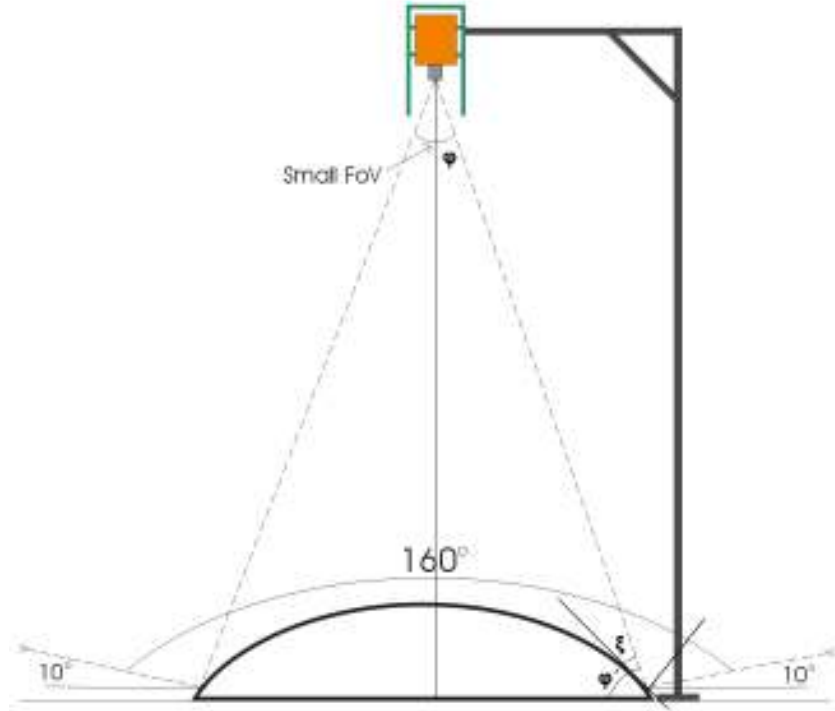


**Figure A. 1**   Plot used for the calculation of parameter *r*.

Then,

$$\varphi + \varphi' + 90 = 180 \Rightarrow \varphi' = 90 - \varphi = 90 - \frac{smallFoV}{2} \qquad \text{(A. 1)}$$

$$\tan^{-1}(\frac{dy}{dx}) = \varphi' - \xi \qquad \text{(A. 2)}$$

where $\frac{dy}{dx}$ is the elevation from the ground of the tangent at the point of reflection

$$180 = \varphi' + 2(90 - \xi) + 10 = 90 - \frac{smallFoV}{2} + 2(90 - \xi) + 10 \Rightarrow$$

$$\Rightarrow \xi = 50 - \frac{smallFoV}{4} \qquad \text{(A. 3)}$$

(A. 1), (A. 2), (A, 3) $\Rightarrow$

$$\tan^{-1}(\frac{dy}{dx}) = 40 - \frac{smallFoV}{4} \Rightarrow \frac{dy}{dx} = \tan(40 - \frac{smallFoV}{4}) \qquad \text{(A. 4)}$$

The small FoV of C3 is $15^{\circ}$. After calculations,

$$\frac{dy}{dx} = 0.7315 \qquad \text{(A. 5)}$$

The mirror is spherical with radius $r$. So,

$$x^2 + y^2 = r^2 \Rightarrow \frac{dy}{dx} = \pm \frac{x}{\sqrt{r^2 - x^2}} \qquad \text{(A. 6)}$$

Then,

$$(\frac{dy}{dx})^2 * (r^2 - x^2) = x^2 \Rightarrow (\frac{dy}{dx})^2 * r^2 = \left[1 + (\frac{dy}{dx})^2\right] x^2 \Rightarrow$$

$$\Rightarrow r = \left| \frac{x * \sqrt{1 + (dy/dx)^2}}{dy/dx} \right| \qquad \text{(A. 7)}$$

But, the reflection point is at the edge of the mirror. So,

$$x = \frac{D}{2} \qquad \text{(A. 8)}$$

(A. 5), (A. 7), (A. 8) $\Rightarrow$ 
$$r = \frac{1.23D}{2 * 0.7315} = \boxed{0.846D} \qquad \text{(A. 9)}$$

## B. 1   The complete code for grabbing and saving MIR images

The grabbing code

```
#include <CyConfig.h>
#include <CyGrabber.h>
#include <CyCameraRegistry.h>
#include <CyCameraInterface.h>
#include <CyImageBuffer.h>
#include <CyDeviceFinder.h>
#include <CyGrayscale8.h>
#include <CyChannel.h>
#include <windows.h>
#include <stdio.h>
#include <CyPixelType.h>
#include <CyTypes.h>


void main();

int main( void )
{
   // An adapter identifier, which is basically a MAC address, is used.
   // A valid ID from the CyAdapterID class is taken.
   CyAdapterID lAdapterID;
   CyAdapterID::GetIdentifier( CyConfig::MODE_UDP, 0, lAdapterID );

   // The main parameters of the Grabber are set.
   printf("Grabber Configuration programmatically.\n");
   lConfig.AddDevice();
   lConfig.SetAccessMode( CyConfig::MODE_UDP );
   lConfig.SetAddress( "[...]" ); // the IP address of the camera is set
   lConfig.SetAdapterID( lAdapterID );  // first Pleora Ethernet card
   lConfig.SetDeviceType( "Standard CameraLink Camera" );
   lConfig.SetName( "Photon Camera" );

   printf("OK with grabber settings!\n");

   //  Set the configuration on the entry to connect to.
   // Here, the device is searched using its name.
   if ( lConfig.FindDeviceByName( "Photon Camera" ) != CY_RESULT_OK )
   {
     // error
     return 1;
   }

   // Connect to the grabber.  It will use the currently
   // selected entry in the config object.
```

```cpp
CyGrabber lGrabber;
if ( lGrabber.Connect( lConfig ) != CY_RESULT_OK )
{  printf("Problem with grabber connection.\n");
   // error
   return 1;
}
else printf("Grabber is connected!\n");


// Create a camera object on top of the grabber.  This camera
// object takes care of configuring both the iPORT and the camera.

// Find the camera type from the configuration.
char lCameraType[128];
lConfig.GetDeviceType( lCameraType, sizeof( lCameraType ) );

// Find the camera in the registry.
CyCameraRegistry lReg;
if ( lReg.FindCamera( lCameraType ) != CY_RESULT_OK )
{
   // error
   return 1;
}
else printf("Camera found in the registry!\n");

// Create the camera.  The previous operation placed the registry
// internal settings on the found camera.  The next step will create
// a camera object of that type.
CyCameraInterface* lCamera = 0;
if ( lReg.CreateCamera( &lCamera, &lGrabber ) != CY_RESULT_OK )
{
   // error
   return 1;
}
else printf("Camera is created!\n");


// Open the dialog window to set the parameters of the camera.
lCamera->ShowDialog(0);


// Create a buffer for grabbing images.
// Get information from the camera which configured from the dialog.
unsigned short lSizeX, lSizeY, lDecimationX, lDecimationY, lBinningX, lBinningY;
CyPixelTypeID lPixelType;
lCamera->GetSizeX( lSizeX );
lCamera->GetSizeY( lSizeY );
lCamera->GetDecimationX( lDecimationX );
lCamera->GetDecimationY( lDecimationY );
lCamera->GetBinningX( lBinningX );
lCamera->GetBinningY( lBinningY );
lCamera->GetEffectivePixelType( lPixelType );

if ( ( lDecimationX != 0 ) && ( lDecimationY != 0 ) && ( lBinningX != 0 ) && ( lBinningY !=
0 ) )
{
   lSizeX = (( lSizeX / lBinningX ) + (( lSizeX % lBinningX ) ? 1 : 0));
   lSizeX = (( lSizeX / lDecimationX ) + (( lSizeX % lDecimationX ) ? 1 : 0));
   lSizeY = (( lSizeY / lBinningY ) + (( lSizeY % lBinningY ) ? 1 : 0));
   lSizeY = (( lSizeY / lDecimationY ) + (( lSizeY % lDecimationY ) ? 1 : 0));
}
```

```
printf("Parameters from the camera are taken!\n");

// Create the buffer using the settings of the MIR camera. Camera and buffer should have the
//same settings.
CyImageBuffer lBuffer( lSizeX, lSizeY, lPixelType );

printf("Buffer is created!\n");


// Grab an image

// First, a data channel from the iPORT IP engine is searched.
CyChannel lChannel;

printf("Channel is created!\n");

if ( lCamera->Grab(  0, lBuffer, 0 ) != CY_RESULT_OK )
{
   // error
   printf("Problem with grabbing!\n");
   delete lCamera; // to avoid memory leak
   return 1;
}
else printf("OK with grabbing!\n");


// Getting the buffer pointer from the CyBuffer class

const unsigned char* lPtr;
unsigned long lSize;
if ( lBuffer.LockForRead( (void**) &lPtr, &lSize, CyBuffer::FLAG_NO_WAIT ) !=
CY_RESULT_OK )
{
   // error handling
   printf("Problem with locking the buffer!\n");
   exit( 1 );

}
else printf("Buffer is locked!\n");

// Now, lPtr points to the data and lSize contains the number of bytes available.
// Here the data is locked and will not be overwritten by
// any other thread.

// Now, data can be saved in the buffer and then used
// The function uses a void** pointer, an unsigned
// char* pointer, because it is more convenient.


printf("Save the image to a file.\n");


if ( lBuffer.Save( "C:\...\...\MIRimage.bmp",  CyGrayscale8::ID , 0x00000002 ) !=
CY_RESULT_OK )
{
   // error handling
   printf("Problem with saving the image!\n");
   exit( 1 );

}
else printf("Image is saved!\n");
```

```
    // Now release the buffer
    lBuffer.SignalReadEnd();

    // The buffer is destroyed.
    lBuffer.~CyImageBuffer();

    // When the connection is not needed, the grabber can be disconnected
    lGrabber.Disconnect();

    delete lCamera;
    printf("The procedure is completed successfully!\n");
    return 0;

}
```

The comments in the code indicate the followed steps. It is useful to analyze important parts of the code.

- CyAdapterID::GetIdentifier( CyConfig::MODE_UDP, 0, lAdapterID );

  The 'MODE_UDP' indicates the IP Engine access mode. It uses the UDP protocol over the Windows Network Stack to communicate with the IP engine. This mode is used because the connection of the Photon Camera is over Ethernet module. The value '0' is unsigned long integer that indicates the zero-based index of the adapter to obtain.

- CY_RESULT_OK

  It is a CyResult code indicating successful execution. Its value is '0'.

- lCamera->ShowDialog(0);

  This command displays the camera configuration dialog. It is an easy way to set all the parameters of the camera. *Figure B.1* shows one tab of the configuration dialog.
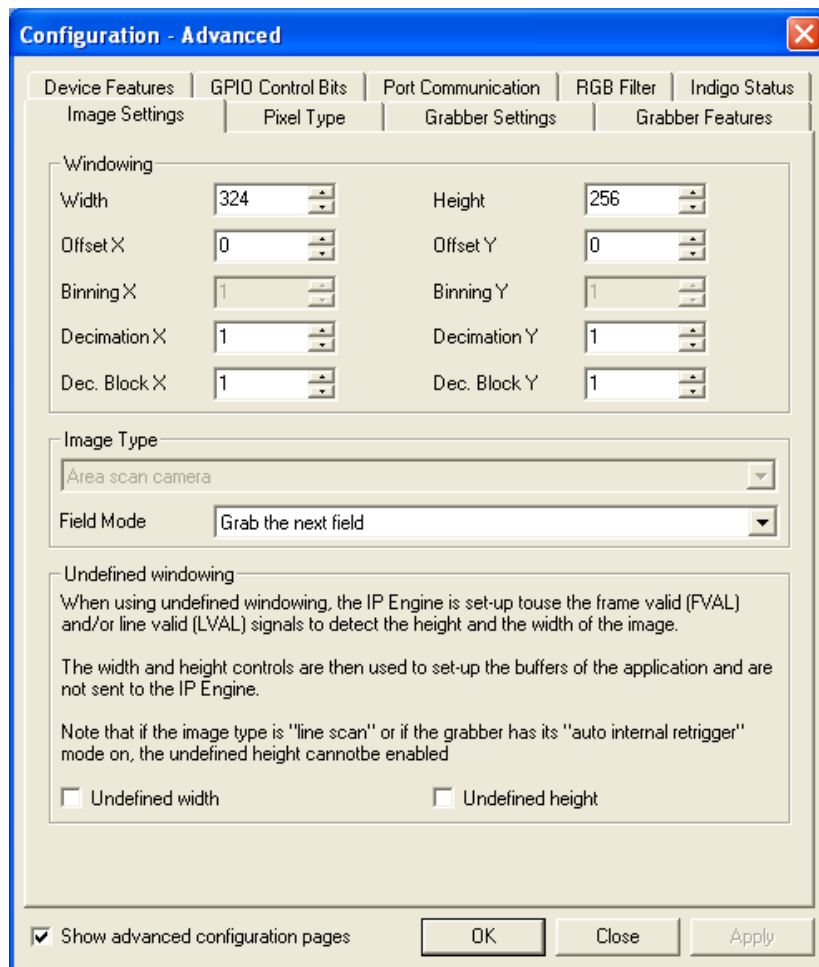
**Figure B. 1** 'Image Settings' tab of the camera configuration dialog.

Pressing the 'OK' or 'Apply' button, the settings are saved and the camera is updated.

- lCamera->Grab( 0, lBuffer, 0)

The value '0' before 'lBuffer' indicates the identification number of the used channel. The command 'CyChannel lChannel;' creates the default channel '0' with no name. The other value '0' shows that no special flag is used for this command.

- CyBuffer::FLAG_NO_WAIT

  If an image is already available, there is no delay for the completion of the next image.

- lBuffer.Save( "C:\...\...\MIRimage.bmp", CyGrayscale8::ID , 0x00000002 )

  The first parameter indicates the directory in which the file will be saved. Moreover, the name of the file is defined. The value 'CyGrayscale8::ID' is used for saving to a windows bitmap. The flag '0x00000002' is another way to express 'FLAG_NO_WAIT' flag.

It is useful to know the time of acquisition in order to create a chronological bar of the cloud coverage. This can be implemented importing the header <time.h> and using the command 'lBuffer.GetReadTimestamp()' which returns the timestamp of the current frame as unsigned long.

## B. 2   The complete code for analyzing the MIR images

The main function 'cloud_coverage_statistics'

```
function cloud_coverage_statistics(direct) % direct = directory of saved MIR images

cd (direct);

% search inside the directory for 'bmp' files exept for the 'mask.bmp'
% and 'filter.bmp' and application of the segmentation method to the found files

h=dir;
a=length(h);
j=0;

for i=1:1:a

  [token, remain] = strtok(h(i).name,'.');
```

```matlab
      name_file=h(i).name;

   if strcmp(remain, '.bmp')==1 && strcmp(token, 'mask')==0 && strcmp(token, 'filter')==0

       segmentation(name_file);  % the segmentation method is called
       j=j+1; %counts the analyzed MIR images

   end

end

% a chronological bar of the cloud coverage is created from the saved images
% and is saved in the same directory

fid=fopen('Coverage.txt','r');
y=zeros(j,1);

for l=1:1:j
   tline = fgetl(fid);
   [tokenl, remainl] = strtok(tline,'     ');
   y(l)=str2double(tokenl);
end

bar(y);
title 'Cloud Coverage of the Hemisphere';
xlabel('Sequence of MIR images');
ylabel('Cloud Coverage of the Hemisphere in %');
saveas(2,'statistics.bmp');


function segmentation(name_file) % name_file = the name of the file that will be analyzed
imIn1 = imread(name_file);
imIn1 = imIn1(1:3:256,1:3:324);

% the filter is loaded and applied on the MIR image
imIn2 = imread('filter.bmp');
imIn2 = imIn2(1:3:256,1:3:324);
k=max(max(imIn2));
for a=1:86
   for b=1:108
      imIn2(a,b)=imIn2(a,b)/k; % the range of values is changed into [0,1]
   end
end
imIn3=imIn1.*imIn2;

% the mask is loaded and applied on the MIR image
imIn4 = imread('mask.bmp');
imIn4 = imIn4(1:3:256,1:3:324);
for c=1:86
   for d=1:108
      if imIn4(c,d)~=0
         imIn4(c,d)=1; % in order to keep the image unaffected after  multiplication
      end
   end
end
imIn=imIn3.*imIn4;

% the image is ready to be analyzed
imOut = Segmentation_Continuum_TD(imIn);

% then, it is displayed
figure(2);
```

```
imagesc(imOut);
colormap(gray);

% the coverage of the sky is calculated and printed on the command window
e=max(max(imOut));
g=length(find(imOut==e));
f=(g/9095)*100;
disp(['Clouds cover the ',num2str(f),'% of the hemisphere.']);

% the analyzed image and the coverage of the sky are saved
name=strtok(name_file,'.');
saveas(2,['SEGMENT_',name],'bmp');
fid=fopen('Coverage.txt','a');
fprintf(fid, '%s\t%s\r',num2str(f),name);
fclose(fid);
```

## The function 'Segmentation_Continuum_TD'

```
function [ imOut ] = Segmentation_Continuum_TD( imIn, cls, bt, perc, kIni, optCls, Tol)

% imIn = Image to be segmented.
% cls = The classes to segment the image, it might be either the number of
% classes or the classes itself. It is the number in of colors in the analyzed image.
% bt = (Optional) Scaling parameter for the cost function.
% perc = (Optional) Percentage of pixels to be reclassified in each
% iteration.
% kIni = (Optional) Conductivity for the non-perturbed problem.
% optCls = (Optional) true to optimize classes values.
% Tol = (Optional) A small values used to stop the algorithm

disp('Image segmentation based on the continuum topological derivative.');
% Total number of finite elements in the image. Mesh nodes are centered in
% the image pixels centers.
  [n,m] = size(imIn);
  imIn = double(imIn);
  if ~exist('cls')
     cls = 2;
  end
  mn = min(min(imIn));
  mx = max(max(imIn));
  if (mn - mx)==0
     error('Image has no information to be segmented!.');
  end
  if length(cls) == 1
     clsVals = mn:(mx-mn)/(cls-1):mx;
     cls = clsVals;
  end
  if ~exist('bt')
  % the smallest the value bt is the more accurate the segmentation is
  bt = 0.0000000000000000000000000001;
  end
  if ~exist('perc')
     perc = 1; % to make the program faster
```

```matlab
        end
    if ~exist('kIni')
        kIni = 1;
    end
    if ~exist('optCls')
        optCls = true;
    end
    if ~exist('Tol')
        Tol = 0.1;
    end
    if optCls
        clsOrg = cls;
    end
% Vector shaped input image.
    v = reshape(imIn, n*m,1);
% Initial guess of the segmented image.
    u = cls(1) * ones(n*m,1);
% Temporary solution.
    uTmp = u;
% As kIni could come from the Restoration_Continuum_TD algorithm, its dimension are checked
% If it is a scalar, new diffusion coeficients for each element are created.
    if (max(size(kIni))==1)
        kElem = kIni * [ones(n*m,1), zeros(n*m,1), zeros(n*m,1), ones(n*m,1)];
    else
        kElem = kIni;
    end
    disp('Preparing linear system...');
% Symbolic elemental matrix.
    IEN = MountIEN(n, m);
% Obtain the global K matrix.
    KG = MountKG(n, m, IEN, kElem);
% Obtain the global M matrix.
    MG = MountMG(n, m, IEN);
    KDir = KG + MG;
% Compute the initial cost function value
    fi = uTmp * 0;
    xi = (fi + (uTmp-v));
    fctmp = ((MulKX(MG, xi)' * xi) + (MulKX(KG, fi)' * fi))/(n*m);
    fc = [Inf, fctmp];
    disp('done. Entering iterative process...');
% For the first iteration.
    minGT = -1;
    it = 1;
    while (abs(fc(it+1)-fc(it))>Tol || minGT < 0)
% Compute the forcing term.
        vu = bt * (v-u);
            f = MulKX(MG, vu);
% Solve the direct problem.
            tol = 1e-8; maxiter = 100;
            fi = pcg(KDir, f, tol, maxiter);
% Solve the adjoint equation.
        lam = ((1-bt)/(bt)) * fi;
% Compute the topological derivative for each element.
            for i = 1:length(cls)
        DT(:,:,i) = reshape(1/2 * ((cls(i) - u) .* ((fi + u - v) + (fi + cls(i) - v) + 2 * bt * lam)), n, m);
            end
% Fixed point algorithm
            [GT, ind] = min(DT, [], 3);
        minGT = min(min(GT));
            [gradSort, jSort] = sort(reshape(GT, n*m, 1));
% Find the pixels that have negative dtopological derivative.
        j = find(gradSort<0);
```

```matlab
                Nchange = round(length(j) * perc);
% Take the class that produced the smaller value for each pixel.
                uTmp(jSort(j(1:Nchange))) = cls(ind(jSort(j(1:Nchange))));
% Auxiliary variable
        xi = (fi + (uTmp-v));
% Compute the cost function value.
        fctmp = ((MulKX(MG, xi)' * xi) + (MulKX(KG, fi)' * fi))/(n*m);
        fc = [fc, fctmp];
% Optimize the classes values?
        if optCls
            [ cls , uTmp] = AdjustClassesValues( cls, uTmp, v, fi, MG, KG);
        end
% Update the result.
        u = uTmp;
        if ~mod(it,5)
            disp(sprintf('Currently at iteration %d.',it));
        end
        it = it + 1;
    end
    imOut = uint8(reshape(u,n,m));
    disp(sprintf('Done in %d iterations.',it - 1));
    if optCls
        disp('Class values optimization was used, initial classes values:');
        disp(clsOrg);
        disp('Optimized values');
        disp(cls);
    end

function [ cn , un] = AdjustClassesValues( co, us, v, fi, MG, KG)
% AdjustClassesValues Adjust classes values in each iteration.
    cn = [];
    for c = co
        fcvd = inf; fcvi = inf;
        xi = (fi + (us - v));
        fcvo = (MulKX(MG, xi)' * xi) + (MulKX(KG, fi)' * fi);
        cl =  min(min(us));
        if c > min(min(us))-1
            cl =  c - 1;
            tmp = us;
            I = find(tmp==c);
            tmp(I) = cl;
            xi = (fi + (tmp - v));
            fcvd = (MulKX(MG, xi)' * xi) + (MulKX(KG, fi)' * fi);
        end
        ci =  max(max(us));
        if c < max(max(us))+1
            ci =  c + 1;
            tmp = us;
            I = find(tmp==c);
            tmp(I) = ci;
            xi = (fi + (tmp - v));
            fcvi = (MulKX(MG, xi)' * xi) + (MulKX(KG, fi)' * fi);
        end

        fct  = [fcvd, fcvo, fcvi];
        ct   = [ cl,   c,   ci];
        [m,i] = min(fct);
        cn    = [cn ct(i)];
    end
% Substitute the new classes values in the segmented image.
    un = us;
    for i= 1:length(co)
```

```matlab
        I = find (us==co(i));
        un(I) = cn(i);
    end


function [ K ] = MountKG( n, m, IEN, kElem)
    nel = (n-1)*(m-1);
    K = sparse(n*m,n*m);
    for i=1:nel
        Kel = MountKel(kElem(i,:));
        K(IEN(i,:),IEN(i,:)) = K(IEN(i,:),IEN(i,:)) + Kel;
    end

function [ kel ] = MountKel( c )
    c11 = c(1); c12 = c(2);     c21 = c(3);         c22 = c(4);
    k1 = (1/12) * (4 * c11 + 3 * c12 + 3 * c21 + 4 * c22);
    k2 = (1/12) * (2 * c11 - 3 * c12 + 3 * c21 - 4 * c22);
    k3 = (1/12) * (-2* c11 - 3 * c12 - 3 * c21 - 2 * c22);
    k4 = (1/12) * (-4* c11 + 3 * c12 - 3 * c21 + 2 * c22);
    kel = [k1, k2, k3, k4;
          k2, k1, k4, k3;
          k3, k4, k1, k2;
          k4, k3, k2, k1];

function [ M ] = MountMG( n, m, IEN)
    Mel = [1/9,1/18,1/36,1/18;
          1/18,1/9,1/18,1/36;
          1/36,1/18,1/9,1/18;
          1/18,1/36,1/18,1/9];
    nel = (n-1)*(m-1);
    M = sparse(n*m, n*m);
    for i=1:nel
        M(IEN(i,:),IEN(i,:)) = M(IEN(i,:),IEN(i,:)) + Mel;
    end

function IEN = MountIEN(n, m)
    IEN = zeros((m-1)*(n-1),4);
    for i=1:m-1
        for j=1:n-1
            IENaux = [idx(j+1,i+1,n),idx(j+1,i,n),idx(j,i,n),idx(j,i+1,n)];
            nel = (n-1)*(i-1)+j;
            IEN(nel,:) = IENaux;
        end
    end

function uxy = Grad(IEN,u)
    for i = 1:size(IEN, 1)
        uloc = u(IEN(i,:));
        uxy(1,i) = ((uloc(2)-uloc(1))+(uloc(3)-uloc(4)))/2;
        uxy(2,i) = ((uloc(4)-uloc(1))+(uloc(3)-uloc(2)))/2;
    end

function id = idx(j,i,n)
    id = n*(i-1) + j;

function [ Ku ] = MulKX( K, u )
    Ku = K * u;
```

The comments in the codes indicate the followed steps and important notes. The value '1:3:256,1:3:324' is used instead of '1:256,1:324' in order to analyze the 1/3 of the pixels. In this way, the program runs faster but there is a loss in data from pixels. What is more, in the main program a matrix *x(l)* containing the time stamps of images can be created and used as the x-axis of the chronological bar. Note that analyzed MIR images saved as matrixes. The biggest value is displayed with white color indicating the presence of cloud and the smallest one with black color indicating clear part of the sky. The code from the function 'Segmentation_Continuum_TD' was found from the web site http://www.mathworks.com.

# Symbols

| Symbol | Nomenclature | Units (SI) |
|--------|--------------|------------|
| a | parameter of the *equation 4.2* | - |
| $a_i$ | saturation with respect to ice | $g/m^3$ |
| $a_s$ | angle of *Figure 5.6* | o |
| $a_w$ | saturation with respect to water | $g/m^3$ |
| b | parameter of the *equation 4.2* | - |
| c | the velocity of light in vacuum, $2.9979 * 10^8$ | m/s |
| d | distance between the camera and the mirror or lens | m |
| D | aperture of the mirror | m |
| e | eccentricity | - |
| h | Planck's constant, $6.6262 * 10^{-34}$ | Js |
| $H_c$ | cloud geometrical thickness | m |
| $h_c$ | cloud altitude | m |
| I | blackbody radiation | W |
| $k$ | Boltzmann's constant, $1.3806 * 10^{-23}$ | J/K |
| $k_h$ | parameter of the *equation 4.4* | - |
| L | dimension of *Figure 3.10* | m |
| $N_c$ | concentration of cloud | $m^{-3}$ |
| r | radius of the spherical mirror | m |
| $r_c$ | mean cloud-droplet size | m |
| $r_h$ | paraxial radius of curvature | m |
| SC | Scwarzschild constant | - |
| T | temperature | K, $^o$C |
| u | thickness of the mirror | m |
| $u_c$ | distance between pinhole and image plane | m |
| $\overline{w}$ | mean water content over the cloud | $g/m^3$ |
| $W_h$ | weight of the hyperbolic mirror | g |
| $w_i$ | ice concentration over the cloud | $g/m^3$ |
| x | loss in FoV due to shading effect | o |
| $x_s$ | cloud area covered by one pixel | m |
| $\lambda$ | wavelength | m |
| $\nu$ | wave number | $m^{-1}$ |
| $\nu_c$ | solid angle of catadioptric system | sr |
| $\varphi$ | angle of *Figure 5.1* | o |
| $\psi$ | angle of *Figure 5.1* | o |
| $\omega$ | angle of *Figure 5.1* | o |

**Table S. 1**  Table of Symbols.

# Abbreviations

| | |
|---|---|
| **Ac** | Altocumulus clouds |
| **AGC** | Automatic Gain Control |
| **As** | Altostratus clouds |
| **Cs** | Cirrostratus clouds |
| **DDE** | Digital Detail Enhancement |
| **FFC** | Flat-Field Correction |
| **FoV** | Field of View |
| **GUI** | Graphical User Interface |
| **HAPS** | High Altitude Platform Station |
| **IP** | Internet Protocol |
| **IR** | Infrared |
| **LVDS** | Low-Voltage Differential Signaling |
| **MIR** | Middle-infrared |
| **NEdT** | Noise Equivalent Temperature Difference |
| **Ns** | Nimbostratus clouds |
| **NTSC** | National Television System Committee |
| **PAL** | Phase Alternating Line |
| **RS-232** | Recommended Standard 232 |
| **SDK** | Software Development Kit |
| **St** | Stratus clouds |
| **UAV** | Unmanned Aerial Vehicle |
| **UDP** | User Datagram Protocol |
| **VDC** | Volts of Direct Current |
| **WMO** | World Meteorological Organization |

# References

[Kar88]    Sherman Karp, Robert M. Gagliardi, Steven E. Moran, Larry B.
           Stotts: OPTICAL CHANNELS fibers, clouds, water, and the
           atmosphere, 1988

[Aus08]    http://www.australiasevereweather.com, 2008

[Wmo08]    http://www.wmo.int, 2008

[Gma07]    http://www.gma.org/surfing/weather/francloud.pdf, 2007

[Fei84]    E. M. Feigelson: Radiation in a Cloudy Atmosphere, 1984

[Zis96]    George J. Zissis: Sources of Radiation vol. 1, 1996

[Jac70]    Herbert Jacobowitz: Emission, Scattering and Absorption of
           Radiation in Cirrus Cloud Layers, 1970

[Bak99]    Simon Baker, Shree K. Nayar: A Theory of Single-Viewpoint
           Catadioptric Image Formation, 1999

[Fli08]    FLIR Systems Inc.: User's manual of the Photon Camera, 2008

[Tho08]    http://www.thorlabs.com/Navigation.cfm?Guide_ID=132, 2008

[Eal08]    Ealing Datasheet from the website
           http://www.ealingcatalog.com, 2008

[Per08]    http://periodic.lanl.gov/default.htm, 2007

[Mel08]    Technical Datasheet from the website
           http://www.mellesgriot.com, 2008